

NUREG/CR-1630  
SAND 80-1794  
R-7

JOINT IN-PILE EQUATION-OF-STATE SERIES ON NUCLEAR FUELS  
AT SANDIA NATIONAL LABORATORIES

W. M. Breitung\*  
K. K. Murata\*\*  
K. O. Reil\*\*  
G. Schumacher\*\*\*

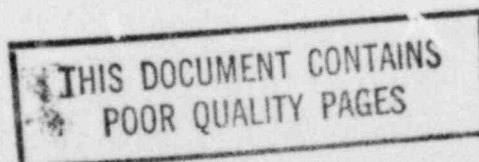
Manuscript Submitted: July 1980  
Date Published: November 1980

Sandia National Laboratories  
Albuquerque, New Mexico 87185  
operated by  
Sandia Corporation  
for the  
U. S. Department of Energy

Prepared for  
Division of Reactor Safety Research  
Office of Nuclear Regulatory Research  
U. S. Nuclear Regulatory Commission  
Washington, DC 20555  
Under Memorandum of Understanding DOE 40-550-75  
NRC FIN No. A 1016

\*On temporary assignment from KfK to Sandia National Laboratories  
\*\*Sandia National Laboratories, USA  
\*\*\*Nuclear Research Center Karlsruhe (KfK), West Germany

8102030667



### ABSTRACT

This report summarizes the EOS work which is related to the new joint Sandia-KfK in-pile series. First, the preceding Sandia-series in the ACPR is described, including in-pile technique, analysis of results, and recommendations for future tests. Then the present status of the joint Sandia-KfK series is given. Emphasis is put on improvements in these new series compared to the first ACPR series. The third part of this report describes the work which is currently underway at KfK: the fabrication of high density uranium oxide crucibles for the in-pile tests. Over 50 figures give a complete overview about experimental techniques, present results and future work.

## TABLE OF CONTENTS

	<u>PAGE</u>
1. Introduction	1
2. First Sandia EOS-Series in the ACPR	2
2.1 In-pile EOS Technique	2
2.1.1 ACPR	2
2.1.2 Experiment Components	3
2.1.3 Data Acquisition and Results	3
2.2 Analysis of Results	7
2.2.1 p-E Relation	7
2.2.2 CO-Formation	9
2.3 Recommendations for Sandia-KfK Series	12
3. Status of Joint Sandia-KfK Series in the ACRR	13
3.1 Program Outline	13
3.2 Improvements of In-Pile EOS Technique	14
3.2.1 ACRR	14
3.2.2 Pressure Cell	15
3.2.3 Calorimeter	16
3.2.4 Contamination Control	17
3.2.5 Data Acquisition	19
3.3 Precalculations	20
4. Fabrication of UO <sub>2</sub> Crucibles at KfK	22
5. Summary	25
6. Literature	28

## 1. INTRODUCTION

Figure 1 summarizes the research programs on Advanced Reactor Safety which are underway at Sandia National Laboratories. These programs address the key phenomena in the various phases of a hypothetical core disruptive accident.

For the accident initiation, and for the disassembly phase, the equation of state of nuclear fuels is an area of major uncertainties. This report summarizes the EOS-work which is relevant to the new joint series of Sandia National Laboratories (SNL) and Kernforschungszentrum Karlsruhe (KfK). This includes:

- the completed SNL-series in the ACPR<sup>(1)</sup> including experimental technique, analysis of results, conclusions for the new series,
- status of the new joint SNL-KfK series in the ACRR presently under preparation at SNL, and
- the supporting work at KfK.

To allow a quick overview, the written text only outlines the main characteristics of the various subjects. The majority of the information is presented in corresponding figures.

## 2. FIRST SANDIA EOS-SERIES IN THE ACPR

The first in-pile EOS-measurements on nuclear fuels were performed at SNL in 1977.<sup>(1)</sup> Because this series represents the basis for the coming joint series, its main features are described in this chapter.

### 2.1 Experimental Technique

About 1 g of uranium oxide was fission-heated within milliseconds to the desired temperature (or energy). The evolved transient fuel vapor pressure was measured with a pressure transducer. The following three paragraphs describe the reactor, the experimental hardware and the data acquisition including the results.

#### 2.1.1 ACPR

The Sandia ACPR, in operation until 1977, is described in Figure 2. Figure 3 shows a picture of the reactor. The ACPR operational characteristics are summarized in Figure 4. Figure 5 shows the ACPR neutron spectrum in the central Experiment Cavity.<sup>(2)</sup> Typical ACPR pulse shapes are given in Figure 6a, together with the fraction of the total energy which is delivered by the pulse tail in Figure 6b.<sup>(2)</sup> The EOS-series used maximum pulses (4.40\$) with a total reactor yield between 94 and 106 MJ. The fraction of the total energy which was delivered in the prompt pulse varies from .79 to .83 (Figure 6b). The corresponding pulse widths (FWHM) varied from 5.3 to 4.9 ms.

### 2.1.2 Experiment Components

The heart of the experiment is the instrumented pressure cell, a cross-sectional view of which is shown in Figure 7. The free volume of about  $300 \text{ mm}^3$  allows for sample expansion during heating and avoids single phase pressures. The free volume was evacuated to .1 Torr. Six thermocouples were located in the graphite crucible (Figure 8) in order to evaluate time dependent heat losses from the fuel sample to the surrounding graphite walls.

The instrumented pressure cell assembly is contained within two sealed cans. Figure 9 shows a cross-section of the complete EEOS in-pile package.

### 2.1.3 Data Acquisition and Results

During an EEOS-experiment, signals from the following instruments were recorded (left side of Figure 10):

- pressure transducer:  $p(t)$ ,
- in-pile Cd self-powered neutron detector: relative reactor power  $P(t)$ ,
- compensated ion chamber (CIC) outside reactor core: zero time  $t_0$
- thermocouples (5 or 8):  $T(t)$  in graphite walls.

These analog data were first recorded on a 14-channel, frequency modulated tape recorder (right side of Figure 10) and later digitized using the CIC-signal as the reference time signal.

From the above data, the desired relation between fuel sample energy and fuel vapor pressure is evaluated in three steps:

A. Radiation noise correction and filtering. The intensive neutron and gamma radiation during a reactor pulse leads to ionization events in instruments and cables which results in radiation noise on pressure and temperature signals. These noise signals were eliminated by irradiating each EOS-assembly twice: once with and once without the fuel sample (Figure 11A and B, respectively). Point by point subtraction of B from A gives the radiation noise corrected signal C. The remaining high frequency noise was then removed with low pass digital filtering techniques (Figure 11D). These filtered and radiation noise corrected signals  $T(t)$  and  $p(t)$  are used in the further evaluations.

B. Fuel sample energy: The second step is determination of the fuel sample energy. The time dependent fuel sample energy  $E_{avg}(t)$  is given by:

$$E_{avg}(t) = E_{total} \times \text{fraction of total energy deposited in the fuel sample at time } t$$

where  $E_{total}$  is the total energy deposited into the sample. Or

$$E_{avg}(t) = E_{total} \times \text{fraction of reactor energy delivered at time } t$$

$$= E_{total} \cdot \frac{\int_{t_0}^t P(t)dt}{\int_{t_0}^{t_e} P(t)dt} \quad (1)$$

The starting time of irradiation  $t_0$  and the relative reactor power  $P(t)$  have been measured,  $t_e$  is the known end time of irradiation.

$E_{total}$  is evaluated by fission product inventory analysis of the  $\gamma$ -emitting nuclei La-140. Because the  $\gamma$ -rays are registered independent of their locus of emission within the sample, the measured  $E_{total}$  is the volume averaged energy deposition in the sample. Equation 1, therefore, gives the volume averaged time dependent sample energy  $E_{avg}(t)$ . However, due to a high fraction of thermal neutrons in the incident neutron flux, a non-neglectable energy deposition gradient exists in the fuel sample. If the ratio of peak to average energy deposition  $P/Avg$  is calculated the peak energy in the fuel sample can be expressed as:

$$E_{peak}(t) = P/Avg \cdot E_{avg}(t) \quad (2)$$

Peak and average energy are shown in Figure 12a for a calculated value of  $P/Avg = 1.19$ .  $E_{avg}(t)$  and  $E_{peak}(t)$  are lower and upper limits, respectively, for the fuel energy which was responsible for the measured pressures.

Figure 12a also depicts the energy loss  $E_{loss}$ , as calculated from thermocouple signals, and the actual average sample energy  $E_{ac} = E_{avg} - E_{loss}$ . The  $E_{loss}(t)$  trace indicates that energy losses out of the sample to the crucible walls are insignificant during the pressure measuring times.



C. Energy-vapor pressure relation: In the third step, a relation between fuel sample energy and fuel vapor pressure is obtained by correlating the noise corrected  $p(t)$  signal with  $E_{avg}(t)$  or  $E_{peak}(t)$ . The first correlation gives a lower energy bound for the actual E-p-dependence (Figure 13). The second correlation yields an upper bound (Figure 14). The resulting band for the energy-pressure relation of  $UO_2$  is shown in Figure 15. The width of this band is determined by the value used for the peak-to-average ratio  $P/Avg$  in Equation 2. In Figure 15 a value of about 1.2 was used. This value was originally calculated in Reference 1 for the initial disk geometry of the sample. Meanwhile additional experimental and theoretical work has revealed that the fuel does change its geometric configuration during the experiment, which results in a time-dependent peak-to-average ratio. The approaches to calculate the ratio  $P/Avg$  will be described below.

The P-E-band of Figure 15 is depicted in Figure 16 in the P-T format together with out-of-pile data for the vapor pressure of  $UO_2$ . Again, it should be kept in mind that the shown high temperature bound of the in-pile measurements is not yet a final result of the EEOS series. Additional analysis is underway to limit the width of the shown band to the pertinent region. Furthermore, a comparison of the in-pile p-E-data with the out-of-pile p-T-data is hindered by the existing uncertainties in the specific heat of liquid  $UO_2$ .

## 2.2 Analysis of Results

### 2.2.1 p-E Relation

An analysis of the measured raw data was initiated in order to determine more precisely the actual fuel energy which was responsible for the pressure signal measured at a given time. The analysis must address movement of the fuel in the available free volume, neutronic energy deposition in the various fuel configurations and heat transfer to the surrounding walls. Since none of the existing HCDA codes is directly applicable to this neutronic-hydrodynamic-heat transfer-problem, three stand-alone codes were coupled. These are TWOTRAN for the neutronic energy deposition into a fixed fuel geometry, CSQ-II for the hydrodynamic movement of liquid and gaseous fuel with a space fixed energy deposition, and TAC-2D for heat transfer in a fixed geometry.

These three codes were initially coupled in the way shown in Figure 17a. This coupling procedure involved the following steps:

- calculation of neutronic energy deposition for the initial fuel disk with TWOTRAN;
- calculation of fuel movement with CSQ, using this energy deposition (Figure 18 and 19);
- recalculation of neutronic energy deposition for different expected fuel geometries (Figure 20 and 21);
- calculation of space and time dependent energy distribution in the sample volume using TAC-2D (Figure 22, Figure 23 shows

results for the fuel disk, Figure 24 for the 100% smeared fuel);  
• correlation of calculated  $E(t)$  with measured  $p(t)$  gives  
bounds for  $p(E)$  (Figure 25).

Figure 26 shows the pressure-energy band which results from the above outlined analysis of the EEOS-experiments.<sup>(3)</sup> The width of this band is composed of two independent contributions:

1. Difficulties in adequately describing the dynamic and inhomogeneous in-pile experiments numerically. For instance, fuel movement is described rather crudely by step-wise dispersal.
2. The scatter which is present in the pressure measurements.

Of the remaining total band width of some 350 J/g, about 150 J/g result from the scatter in the experimental data; the other 200 J/g originate in the uncertainties in the analytical modeling.

Further efforts in reducing these modeling uncertainties of 200 J/g (about  $\pm 6\%$  in energy) showed that calculation of the fuel movement is the crucial step in the above code coupling scheme. The reasons are two-fold: (1) fuel movement is a very effective energy transport mechanism and (2) fuel movement has a strong influence on the neutronic energy deposition due to changing self-shielding effects in the fuel. Therefore, the improved coupling scheme of Figure 17b, which accounts for the strong interaction of fuel movement and fuel energy distribution, is presently under study. The basic idea of

this new scheme is simple: the input EOS into CSQ-II is iterated until the calculated dynamic pressure matches the measured one.

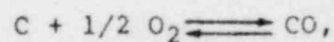
The numerical realization of this scheme, however, is not simple and requires extensive code development. The main problems with CSQ-II currently being addressed are:

- the spatial resolution is limited due to excessive running times;
- only space fixed energy deposition is possible;
- truncation errors in the difference equations lead to unacceptable numerical mixing of hot and cold fuel regions.

Even with substantial code development, it is unreasonable to expect that fuel energies can be calculated to better than  $\pm 3\%$ . Such a level of uncertainty is, however, acceptable in view of the experimental scatter, which corresponds to about  $\pm 5\%$  in the fuel energy.

### 2.2.2 CO-Formation

The EEOS series used a pressure vessel with an inner graphite liner. At the high temperatures involved, graphite can oxidize to gaseous CO using oxygen from the oxide fuel. The pressure of CO is determined by the reaction equation



giving

$$P_{\text{CO}} = \sqrt{P_{\text{O}_2}} \cdot \exp \left[ - \frac{\Delta G^{0,T}(\text{CO})}{RT} \right]$$

where

$$P_{O_2} = \exp \left[ \frac{\Delta G_{O_2}^{o,T}(U, PuO_{2+x})}{RT} \right]$$

From this equation, CO-equilibrium pressures result as shown in Figure 27. The data for  $\Delta G^{o,T}(CO)$  were taken from Reference 4 and those for  $\Delta G_{O_2}^{o,T}(U, PuO_{2+x})$  from Reference 5. The pressures are very high indeed, if equilibrium can be reached during the experiment. Thus CO generation could cause an additional, non-prototypical contribution to the measured fuel vapor pressure. Consequently, the kinetics of CO-formation were investigated.

Build-up of a CO-pressure within the EOS capsule involves three steps:

- a) The diffusion of oxygen via the gaseous phase to the graphite walls or out of liquid fuel which is in contact with graphite;
- b) the reaction of oxygen with graphite at the graphite surface; and
- c) the release of the reaction product CO into the graphite container volume.

A thorough investigation of this combined mass transfer problem is hindered by the unknown reaction kinetics of atomic oxygen with graphite. Therefore, it was decided to examine only process a), the possible oxygen diffusion fluxes. The resulting CO-pressure histories are consequently upper estimates for possible CO pressures.

The oxygen transport was investigated for two fuel geometries, a quiescent layer of liquid fuel resting on the container bottom (slab geometry, Figure 28a) and a system of homogeneously distributed liquid droplets of uniform radius (droplet geometry, Figure 28b). The various calculation parameters are summarized in Figure 30, and Figure 31 shows the corresponding calculated CO-pressures as a function of time. Using the CSQ, TAC-2D and PIE results, which became available meanwhile, it was possible to reduce the parameter space covered in Figure 31 to the pertinent region.

In the slab geometry, for instance, contact temperatures of 3380 K (curves 6 and 7) are not reached. Instead a frozen  $UO_2$ -layer of about 30  $\mu m$  thickness is calculated which acts as an effective barrier for oxygen and CO transport. In the case of droplet geometry, the temperatures in the diffusion boundary layer are around 4000 K only, and average droplet sizes range around  $10^{-4}$  m. Thus, curve 15 ( $R_f = 10^{-4}$ , 4000 K) seems the appropriate one to describe the maximum possible CO-formation during an EEOS experiment. However, not only oxygen is transported to the graphite walls but also fuel vapor, which condenses and forms a protective oxide liner. Such a vapor deposit oxide layer was seen in the post irradiation examinations.

In summary, with and without fuel dispersal no significant CO-formation from fuel-crucible reactions is expected during the EEOS measurements.

### 2.3 Recommendations for Sandia-KfK Series

The experience gained from the above described analytical efforts has been used in the design of the new joint Sandia-KfK EOS series which will be performed in the upgraded reactor ACRR. The recommendations are summarized in Figure 32. First priority has obtainment of the flattest energy deposition profile possible. Proper measures are neutron filtering, shadowing neutron absorbers, and the use of fuel powder. The use of powder has the additional advantage that no large free volumes are available for gross fuel movement, and nevertheless single phase pressures from liquid fuel are avoided. Other improvements include the use of an oxide liner and an advanced preparation route of EOS experiment parts which will be described below.

### 3. STATUS OF JOINT SANDIA-KFK SERIES IN THE ACRR

#### 3.1 Program Outline

Table I shows the planned EOS series as sponsored by Sandia-NRC and KfK-PSB, respectively.

TABLE I

Sponsor	Number of Experiments On			
	UO <sub>2</sub>	UC	(U,Pu)O <sub>2</sub>	
	fresh	fresh	fresh	irradiated
Sandia (NRC)	1	4	---	3
KfK (PSB)	2	---	2	---

The individual funding is complementary. The joint test matrix covers all nuclear fuels of interest and allows a steady development of experimental techniques, starting with more straightforward fresh UO<sub>2</sub> experiments and ending with the difficult tests on irradiated (U,Pu)O<sub>2</sub>. These in-pile experiments address the following open questions:

- What is the true vapor pressure of nuclear fuel under HCDA heating conditions, i.e., neutronic heating in some milliseconds?
- Do these heating conditions create new phenomena like low dynamic heat capacities, molecular dissociation or



ionization, which result in genuine higher vapor pressures than those of out-of-pile experiments?

- Were the high pressures in the closed-system Sandia experiments (Figure 16) due to non-fuel pressure sources, which are related to experiment preparation and design, like fuel contamination or crucible outgassing?

### 3.2 Improvements of In-Pile EOS Technique

Since the first in-pile EOS experiments were performed at Sandia<sup>(1)</sup>, a number of improvements on this technique have become possible. Advances and present status of the joint Sandia-KfK series is given below.

#### 3.2.1 ACRR

The ACRR became operational August 25, 1978. Figure 33 shows the ACRR core configurations. The operational characteristics for pulse and steady-state mode are summarized in Figure 34. Figure 35 depicts the neutron spectrum in the bare experiment cavity. Figure 36 gives an idea about the energy deposition capabilities in the ACRR. The flexible control system of the ACRR allows a number of advanced operational modes, as depicted in Figure 37. Some of them are not yet ready for use but will become available in the near future. Figure 38 finally compares the ACRR performance characteristics to those of the old ACPR. Most important for EOS-experiments is the increased pulse fluence (by a factor of 3.2 over the ACPR) which will allow filtering of thermal neutrons and very flat energy deposition profiles in the fuel samples. (See paragraph 3.3).

### 3.2.2 Pressure Cell

Compared to the pressure cell described in paragraph 2.1.2, the following improvements will be made in the new SNL-KfK series:

- A. Fuel: 1 g of fuel powder of .1 to .3 mm particle sizes will be used. Fuel density will be about 50% of the theoretical density, which is typical for the fuel smear density in the voided LMFBR core. A more appropriate fuel stoichiometry will be used; namely,  $\text{UO}_{2.00}$  and  $(\text{U.Pu})\text{O}_{1.97}$ .
- B. Crucible: The use of high-density  $\text{UO}_2$  crucibles excludes non-fuel pressure sources from the crucible or from fuel crucible chemical reactions. In addition, heat losses are reduced, compared to graphite crucibles, due to the low thermal conductivity of  $\text{UO}_2$ . For crucible fabrication see Chapter 4. The experiments on UC will use pyrolytic graphite as crucible material, which has several advantages over the previously used isotropic graphite.
- C. Pressure Transducer: To facilitate interpretation of the pressure transducer signal in the case of uneven loading of the transducer diaphragm, a specially shaped washer will be inserted. By this means, the pressure transducer signal is proportional to the total force acting on the crucible lid, independent of the lateral force distribution across the lid.

In addition, undesirable thermal bowing effects of the crucible lid will not falsify the transducer signal.

D. Cell Closure and Reopening: A new, simpler sealing element of the EOS pressure cell will be used. In addition, a changed design will allow reopening of the capsule in a UHV-system after the experiment, in order to analyze the residual gases mass spectrometrically.

E. Neutron Filters: Neutron filters will be added to the EOS pressure cell in order to further decrease the energy deposition gradients in the fuel sample.

### 3.2.3 Calorimeter

For the new EOS-series, an in-pile calorimeter was designed. Its purpose is to give an independent, absolute and high precision measurement of the total energy deposited in the fuel during an EOS experiment. Its performance will be tested in the fresh fuel experiments by comparison with the previously described fission product inventory analysis. In the irradiated fuel tests, the calorimetric energy deposition measurement will be the only possible method to determine the total energy deposition into the fuel sample ( $E_{\text{total}}$  in Equation 1). Figure 39 shows a cross-section of the present calorimeter design. To minimize energy deposition differences in calorimeter and EOS-cell fuel, calorimeter and EOS-cell are designed as similar as possible. The calorimeter investigations done so far include heat losses, stress analysis of the copper body, instrumentation, and background from neutron and  $\gamma$ -heating of copper. A remaining

point is the calculation of the differences of the neutron,  $\beta$ - and  $\gamma$ -absorption in the calorimeter fuel compared to the EOS fuel. Figure 40 summarizes the calorimeter data of interest.

#### 3.2.4 Contamination Control

Because EOS experiments in a closed volume are very sensitive to contamination, a cleaning and handling procedure was designed for the EOS experiment components.<sup>(6)</sup> The first step was identification of sources for contaminant pressures in EOS experiments (sources D and E in Figure 41). The estimated contributions of the various pressure sources in Figure 41 demonstrate that contamination pressures can easily invalidate fuel pressure measurements. An important pressure contribution can also arise from prototypical fuel impurities like C, N<sub>2</sub>, and H<sub>2</sub>O, which are introduced during the fabrication process. It should be added here that this reactor-typical pressure source is seen in the described closed-system in-pile experiments but not in open-system experiments like laser evaporation or transpiration method (see Figure 16).

The goal of the designed preparation route is to keep contamination from handling below the resolution of the used pressure transducer. This corresponds to about 1  $\mu$ mol of contaminant gases or 3 monolayers of contamination on the fuel surface.

Of the various contamination sources, physisorption of gases was investigated in detail because this process can result

in multilayer formation on exposed surfaces. A kinetic adsorption model was set up to estimate for which gases and which conditions (p,T) multilayer physisorption has to be expected (Figure 42). Capable of multilayer adsorption during the experiment preparation are gases having high heats of physisorption and a critical temperature above 300 K. The most important gases of this class are water vapor and polar hydrocarbons. The kinetic model predicts that at room temperature partial pressures less than 1 Pa (= 10 ppm at 1 bar) of these gases are required to keep the surface coverage below one monolayer. Other gases are not critical for the contamination of EOS experiment parts.

Figure 43 gives a complete list of contamination sources, expected contaminants and planned cleaning steps. Cleaning is designed to take place in three different environments with increasing degree of cleanliness. Because physically adsorbed multilayers of water and hydrocarbons are expected to be major causes for contamination, the last two cleaning steps specifically aim at removal of these compounds. The flow of pressure cell components through the various stages of cleaning and processing is summarized in Figure 44. Figure 45 shows processing steps of fuel and loaded EOS pressure cell. After the final bake-out, the EOS cell will be closed under vacuum within a special UHV-mounting system (Figure 46). After the experiment, the pressure cell will be reopened in this system to analyze amount and composition of the residual gases.

### 3.2.5 Data Acquisition

The data acquisition system currently used for Accident Energetics Work is shown schematically in Figure 47. This system is located in the ACRR Low Bay adjacent to the reactor facility. As shown, data may be recorded on FM tape recorders (26 channels of data), displayed on a viscorder oscillograph, and digitized by high speed analog to digital converters (ADC's) in the Data Acquisition and Display System (DADS) terminal. The system contains provisions for complete system calibration. Pressure transducer electronics, thermocouple reference junctions, and reactor power instrumentation are located at the reactor and are connected to the data acquisition by a permanent cable bus.

The Station 1 DADS terminal is shown schematically in Figure 48. The terminal is built around an HP9845 desk top calculator with 449 K bytes of memory. Analog input is via eight high speed ADC channels with a maximum sampling rate of 400 kHz. Each input may be multiplexed 2 or 4 times for sampling rates less than or equal to 40 kHz. Each ADC channel has an associated 32768 word external memory. The calculator may read the external ADC memories, perform limited computation, display the data, store data on a cartridge disc or transmit the data to the central DADS computer. The central DADS computer provides additional computational capability along with digital magnetic tape data storage and a better graphics plotter.

### 3.3 Precalculations

The current design objective for the new EOS experiments is an energy uncertainty of  $\pm 4\%$ . This objective appears possible in the ACRR, at least for fresh fuel, through careful neutronic design. Extensive TWOTRAN neutron transport calculations, discussed below, suggest a 4 to 7% peak to average energy deposition ratio is possible for a thin shielded disk-shaped cavity filled with powdered fuel. The "predispersed" powder configuration should minimize the changes in energy profile with geometry found in the first series. Estimates of heat transfer effects suggest that these will not be important in determining the lower internal energy bound for the fuel during the pressure measurement times for the present geometry. Thus, the energy uncertainties after analysis should be bounded by the peak and average energy deposition values.

The TWOTRAN neutron transport calculations incorporate a short cylindrical gold filter positioned as shown in Figure 49 some distance from the fuel disc. The filter in this geometry is primarily a solid angle occluder; the isotropic flux in the filter midplane in the absence of the fuel disc decreases as a function of radius from solid angle considerations. The normal increase in fission density with radius in the fuel disc can thereby be offset and even reversed. Although TWOTRAN is not capable of more elaborate occluder designs, one could in principle consider split ring and double ring designs to gain more flexibility in tailoring the radial profile.

The thickness of the fuel disc can be adjusted to minimize the axial variation of the energy deposition, but of course, the practical lower bound is determined by heat transfer considerations.

A test case TWOTRAN calculation for the geometry in Figure 49 gives a radial variation for the energy deposition in the fuel disc as shown in Figure 50. This calculation corresponds to 1 gm of 15% enriched UC fuel at 50% density and a gold occluder nominally 1 cm high and 0.15 cm thick. A lower Inconel plate is included in the calculation to assure top-to-bottom symmetry along with top and bottom polyethylene reflectors (not shown) and a tall cylindrical polyethylene moderator (not shown). The bands for different moderator thicknesses represent the probable peak-to-minimum axial variation at given radius. The TWOTRAN results for the profile will be verified by performing dosimetry on a uranium metal calibration sample formed of nested rings.



#### 4. FABRICATION OF $UO_2$ CRUCIBLES AT KFK

Recently an apparatus has been developed which allows the fabrication of crucibles of high temperature materials. This apparatus works on the basis of hot pressing units which produce exact shaped pieces of materials of high density by sintering under high pressures and temperatures in a heated graphite die. It is the appropriate equipment for fabrication of the  $UO_2$  crucible placed inside the pressure capsule for the EOS experiments in the ACRR. Crucibles with dimensional tolerances specified for these capsules cannot be produced by normal sintering techniques in which cold pressed shapes are sintered at high temperatures of 1900-2000 K. Internal stresses of the cold pressed crucible would influence the shrinking during sintering and cause irregularities and material cracks. Such stresses cannot build up during hot pressing because of the plastic state of the hot material. Furthermore, the shape of the specimen is exactly given by that of the die.

The principle of the equipment used is sketched in Figure 51. The graphite die is placed between the two hydraulic cylinders of the press. It is depicted in the center of the Figure 51, surrounded by the induction coil. The position of the hot pressed crucible inside the die is represented by the dotted area between the upper and lower piston. A sealed silica glass cylinder around the die allows working under vacuum and inert gas atmosphere. The outer part of the upper piston is sealed at the cover plate by a Viton O-ring.

This part of the piston is cooled at its connection to the upper hydraulic cylinder to prevent heating of press and O-ring. The inner part of the piston is inserted into the outer one with thermal insulation to minimize heat losses.

The base plate carries all parts of the apparatus which do not move. These are the sealed silica tube and the lower piston which determines the inner diameter of the crucible. Three columns penetrate the base plate through sealed feed-throughs and transmit the pressure of the lower hydraulic system to the pressure plate which acts on the graphite die via alumina tube and disks on which the die is placed. Thus, the graphite die and the upper piston can be moved by two independent hydraulic cylinders. This allows to impose different loadings on the bottom and the wall of the crucible during sintering. The downward movement of the upper piston compacts the bottom of the crucible by pressing the  $UO_2$  powder against the fixed lower piston. Upward movement of the graphite die compacts the crucible wall by pressing the  $UO_2$  against the upper piston (Figure 52).

The process of fabrication starts by filling up the graphite die with  $UO_2$  powder. The die sits on the alumina plates and surrounds the lower piston which ends in the upper third. Appropriate quantities of powder are stamped into the wall and bottom regions. Upper piston and silica tube are inserted and sealed. After heating up the die by high frequency induction to  $1700^\circ C$ , pressures of 100 and 150 MPa are imposed

to the die and the upper piston for five minutes. Before cooling, the upper load is removed and the die is pushed upwards to draw the lower piston out of the sintered crucible. This prevents the crucible from shrinking onto the piston which would cause cracking of the walls. Figure 52 reveals that the crucible is in contact with graphite at its outer surface and with tungsten at its inner surface. Therefore, contamination with carbon should be minor inside the crucible. Surface contaminations are removed by heating the crucible under vacuum with an oxygen partial pressure of some  $10^{-4}$  atm in an atmosphere free of hydrocarbons. The crucible density is higher than 95% of the theoretical density. Thus, the pores are closed and transport of gases out of or into the crucible walls during the reactor experiment is not possible. Because of the high surface quality of the tungsten piston, which is not influenced during hot pressing, the inner wall surface of the crucible is smooth and needs no further machining. The  $UO_2$ -piston has to be machined at its sliding surface to fit it to the inner crucible diameter.

A drawing of the  $UO_2$ -crucible and  $UO_2$ -piston to be produced is given in Figure 53; a photograph of one of the hot pressed crucibles is shown in Figure 54.

## 5. SUMMARY

The EOS work which is related to the new joint SNL-KfK in-pile EOS series is summarized. An introduction is given in Chapter 1.

Chapter 2 describes the experimental features of the first in-pile SNL series on nuclear fuels (Figures 2 to 11) since this in-pile technique represents the basis for the coming joint series. The present results of this first series on  $UO_2$  are the following:

- The p-E-relation was measured for the average energy deposition into the sample with an experimental scatter corresponding to about  $\pm 5\%$  in average energy. However, an additional uncertainty arises from the uneven energy deposition in the sample (around  $\pm 12\%$ ).
- Analysis of these additional uncertainties requires coupled neutronic-hydrodynamic-heat transfer calculations. The first coupling scheme of three standalone codes resulted in about  $\pm 6\%$  in the energy. Extensive code development is presently underway to further reduce this uncertainty contribution by use of an improved coupling scheme. However  $\pm 3\%$  appears to be the lowest achievable level of analytical energy uncertainty.
- CO-formation from graphite- $UO_2$  reactions during the pressure measuring times was insignificant (Figure 31).
- Several recommendations for the new series resulted from the analysis (Figure 32).

Planning and status of the new joint in-pile series are given in Chapter 3. Table I on page 13 shows the planned test matrix. Improvements of the in-pile technique are concerned with:

- the new reactor ACRR (Figures 33 to 38),
- a new pressure cell design,
- an in-pile calorimeter for an absolute and high precision measurement of the total average energy deposition (Figure 39),
- a carefully designed preparation route to keep pressure contributions from handling contaminations below the resolution of the pressure transducer (Figures 41 to 46),
- additional data acquisition capabilities of the new DADS system.

Precalculations for the coming UC-series using neutron transport codes suggest that the energy deposition variations in the sample can be kept below  $\pm 4\%$  (Figures 49 and 50) by proper experiment design (neutron filters, fuel powder).

Chapter 4 describes the fabrication of  $\text{UO}_2$ -crucibles for the coming oxide series which is presently underway at KfK-INR. The recently completed Hot Pressing Apparatus (Figures 51 and 52) allows fabrication of high-density crucibles with extremely high dimensional precision without additional machining ( $\pm 0.025$  mm,  $\pm 0.001$  inch). Figure 54 shows one of the first crucibles obtained with the Hot Pressing Apparatus.

#### ACKNOWLEDGEMENT

Many of the hydrodynamic calculations described in Paragraph 2.2.1 were done by Elaine Gorham-Bergeron, presently on leave to Centre d'Etudes Nucleaires in Cadarache, France.

## LITERATURE

1. K. O. Reil, Effective Equation of State Measurements on Uranium Dioxide, Dissertation, Nucl. Eng. Dept., University of New Mexico, Albuquerque, New Mexico (May 1977).
2. L. L. Bonzon, F. M. Morris, F. V. Thorne, Annular Core Pulse Reactor (ACPR): Experimenters Manual, Report SLA-73-1017 (October 1974).
3. W. Breitung, E. Gorham-Bergeron, K. K. Murata, "Analysis of Sandia In-Pile EOS Experiments," Proc. of the International Meeting on Fast Reactor Safety Technology, Seattle, Washington, August 19-23, 1979, p. 1059-1068.
4. Rep. NSRDS-NBS37, JANAF Thermochemical Tables, 2. Ed.
5. M. Eober, W. Breitung, H. U. Karow, G. Schumacher, Calculation and Experimental Estimation of the Equation of State of Irradiated Fuel, IAEA, IWGFR/79, Harwell, UK, June 28, 1977.
6. W. Breitung, Contamination Control in Sandia Equation of State Experiments, Report SAND80-1277, in print.

FIGURE 1. SANDIA LABS FY80 PROGRAM BREAKDOWN  
ADVANCED REACTOR SAFETY RESEARCH

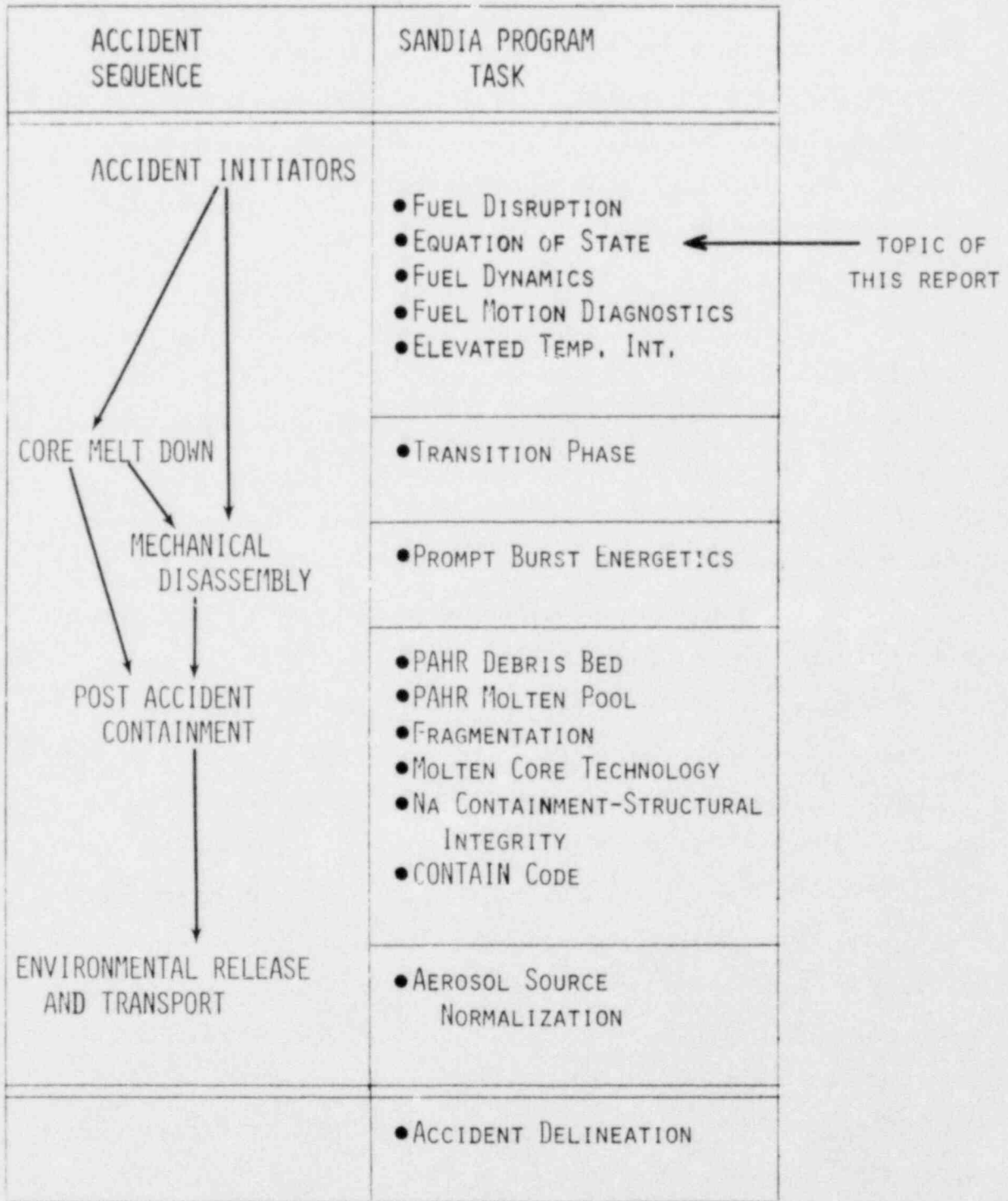




Figure 2. ACPR DESCRIPTION (2)

The ACPR (Figure 3) is a TRIGA-type reactor utilizing stainless-steel-clad uranium/zirconium-hydride (ZrH) fuel elements, but with a dry experiment cavity 23 cm in diameter occupying the central region of the core. The core structure is at the bottom of a stainless-steel-lined water-filled tank 3.05 m in diameter and 8.5 m deep. The top of the core is 7.0 m below the water surface.

The core contains fuel-moderator elements in which a ZrH moderator is homogeneously combined with enriched uranium fuel. The active section of this fuel-moderator element is 38.1 cm in length by 3.56 cm in diameter and contains 12 weight percent uranium and 88 weight percent zirconium hydride. The 12 weight percent uranium is enriched to 20 percent in  $^{235}\text{U}$  and the hydrogen-to-zirconium atom ratio of the ZrH moderator material is 1.625 to 1. Graphite cylinders 8.8 cm in length by 3.56 cm in diameter act as top and bottom reflectors.

Six motor-driven control rods govern reactor power during delayed critical operations.

The adjustable transient rod on the ACPR is actuated by an electro-pneumatic system. The mechanical drive system permits the adjustable transient rod to be used in the steady-state as well as the pulse mode of operation. In the pulse mode the adjustable drive system is used to adjust reactivity so that pulses of any size may be obtained up to the maximum reactivity worth of the transient rod system.

Although the ACPR core still exists the reactor has been dismantled and replaced by the ACRR.

POOR ORIGINAL

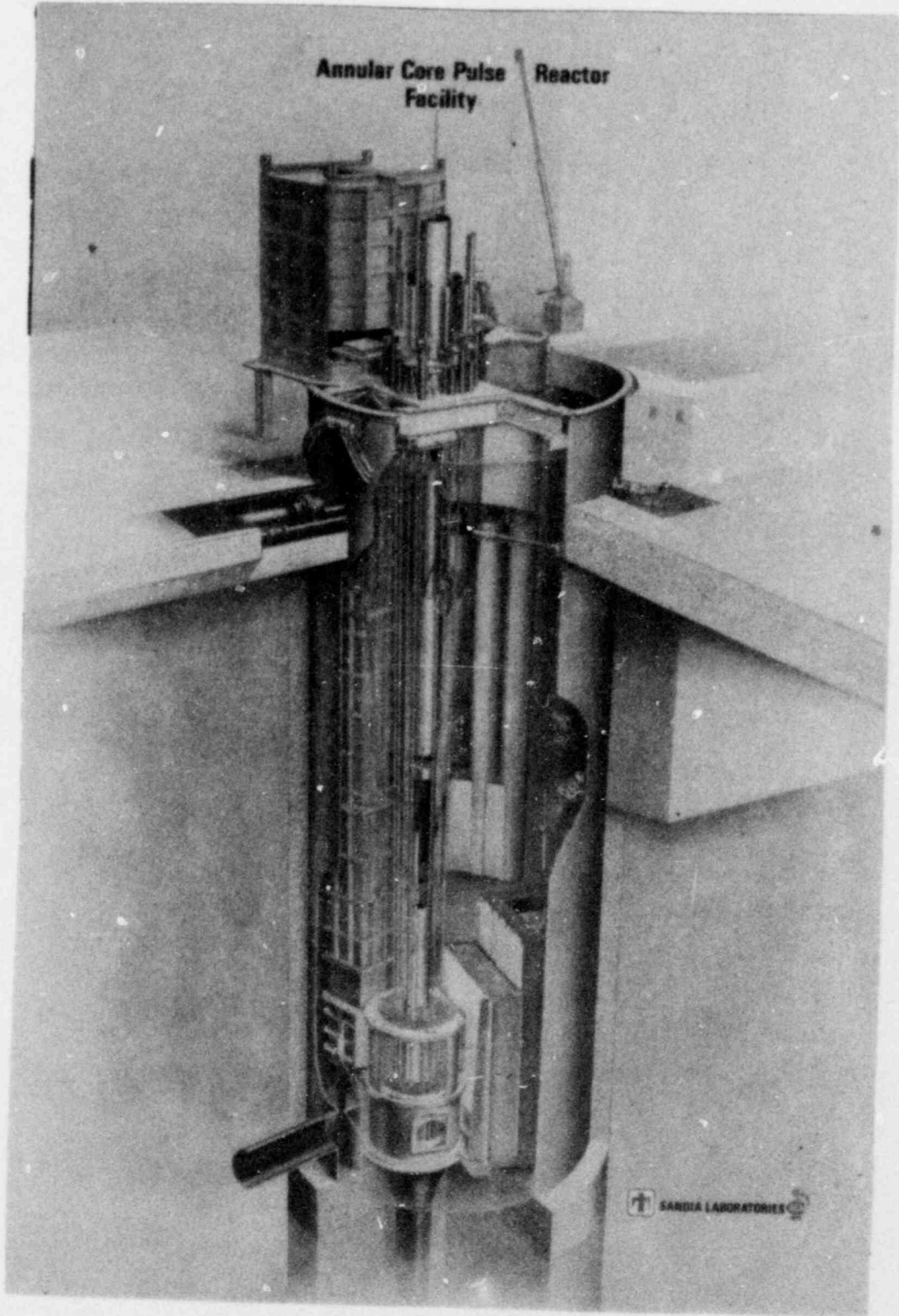


Figure 3. Cross-Sectional View of the ACPR

**Figure 4.** ACPR Operational Characteristics  
(Cavity Horizontal and Vertical Centerline, Free-Field)

Pulse Operations:

Reactivity Inserted	\$4.40
Peak Power	14000 MW
Pulse Width (FWHM)	4.7 msec
Reactor Period	1.3 msec
Maximum (Recorded) Fuel Temperature	750° C
Energy Release	~108 MW-sec

Neutron Dose:

> 10 keV	$1.0 \times 10^{15}$ n/cm <sup>2</sup>
Maximum rate (> 10 keV)	$2.5 \times 10^{17}$ n/cm <sup>2</sup> -sec
All Energies	$2.0 \times 10^{15}$ n/cm <sup>2</sup>
Thermal (< 0.4 eV)	$7.8 \times 10^{14}$ n/cm <sup>2</sup>

Gamma Dose:

Total Dose	$10^6$ rads (H <sub>2</sub> O)
Maximum Rate	$2.1 \times 10^8$ rads (H <sub>2</sub> O)/sec

Characteristics of Steady-State Operation:

Power	300 kW
Neutron Flux (> 10 keV)	$2.8 \times 10^{12}$ n/cm <sup>2</sup> -sec
Neutron Flux (All Energies)	$0.57 \times 10^{13}$ n/cm <sup>2</sup> -sec
Gamma Dose Rate	3300 rads (H <sub>2</sub> O)/sec

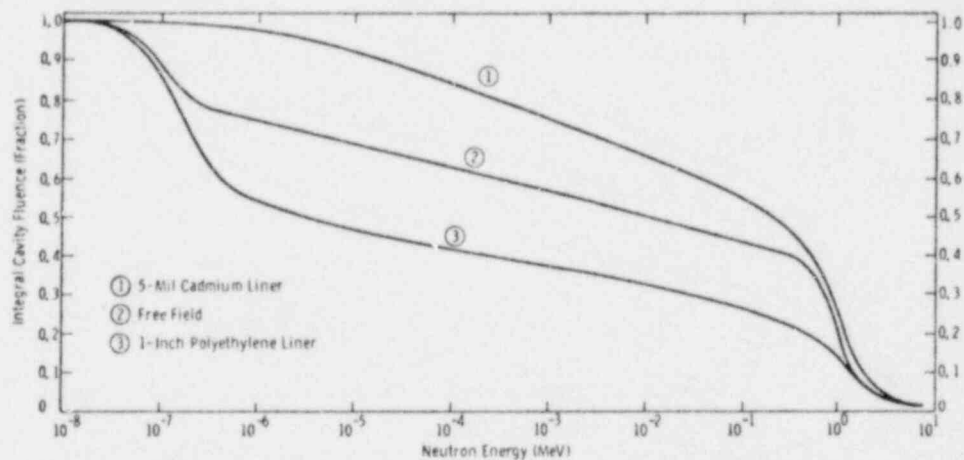


Figure 5. Integral Cavity Fluence for all Neutron Energies, Showing the Effects of Spectral Modifications

ACPR Cavity Spectra

Group	Lower Limit Energy of Group	Free-Field Normalized Differential Spectrum	Normalized Integral Spectrum		
			Free-Field	2.54 cm Polyethylene	0.0127 cm Cadmium
1	3 MeV	0.033	0.033	0.03	0.05
2	1.4	0.084	0.117	0.10	0.14
3	0.9	0.113	0.230	0.15	0.28
4	0.4	0.139	0.369	0.21	0.44
5	0.1	0.071	0.440	0.26	0.55
6	17 keV	0.050	0.490	0.31	0.64
7	3	0.047	0.537	0.35	0.71
8	0.55	0.044	0.581	0.39	0.77
9	100 eV	0.041	0.622	0.42	0.84
10	30	0.033	0.655	0.44	0.88
11	10	0.029	0.684	0.47	0.92
12	3	0.036	0.720	0.51	0.95
13	1	0.029	0.749	0.54	0.97
14	0.4	0.024	0.773	0.61	0.98
15	0.1	0.122	0.895	0.86	0.99
16	Thermal	0.107	1.0	1.0	1.0

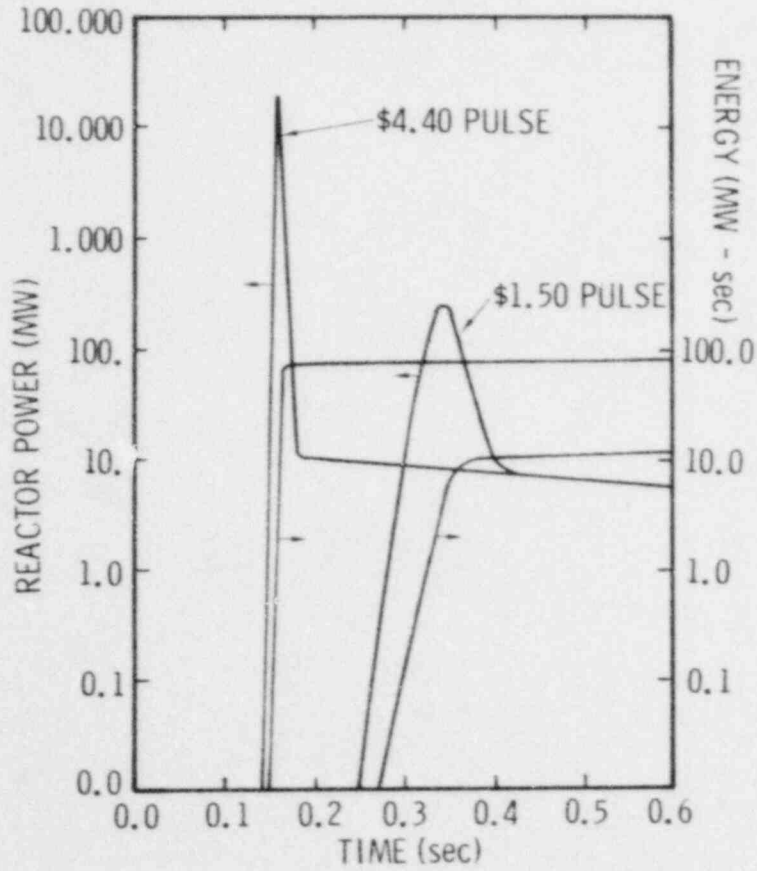


Figure 6a.

Typical ACPR Pulse Shapes  
and Corresponding Pulse Integrals

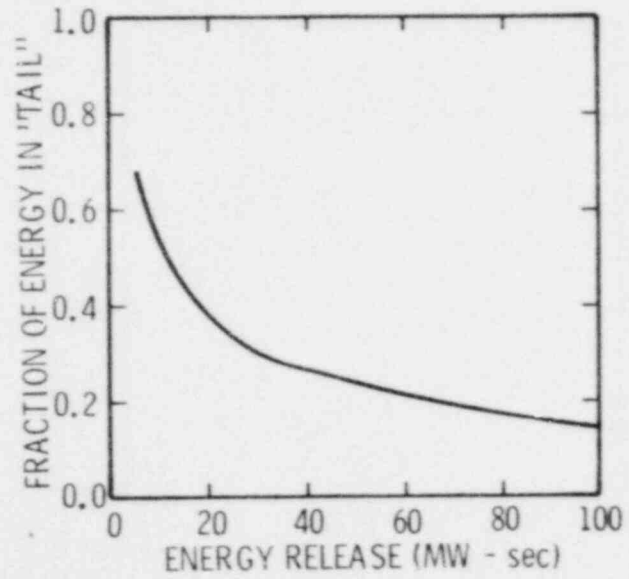


Figure 6b.

Fraction of Energy in Pulse Tail  
Vs. Total Pulse Energy Release

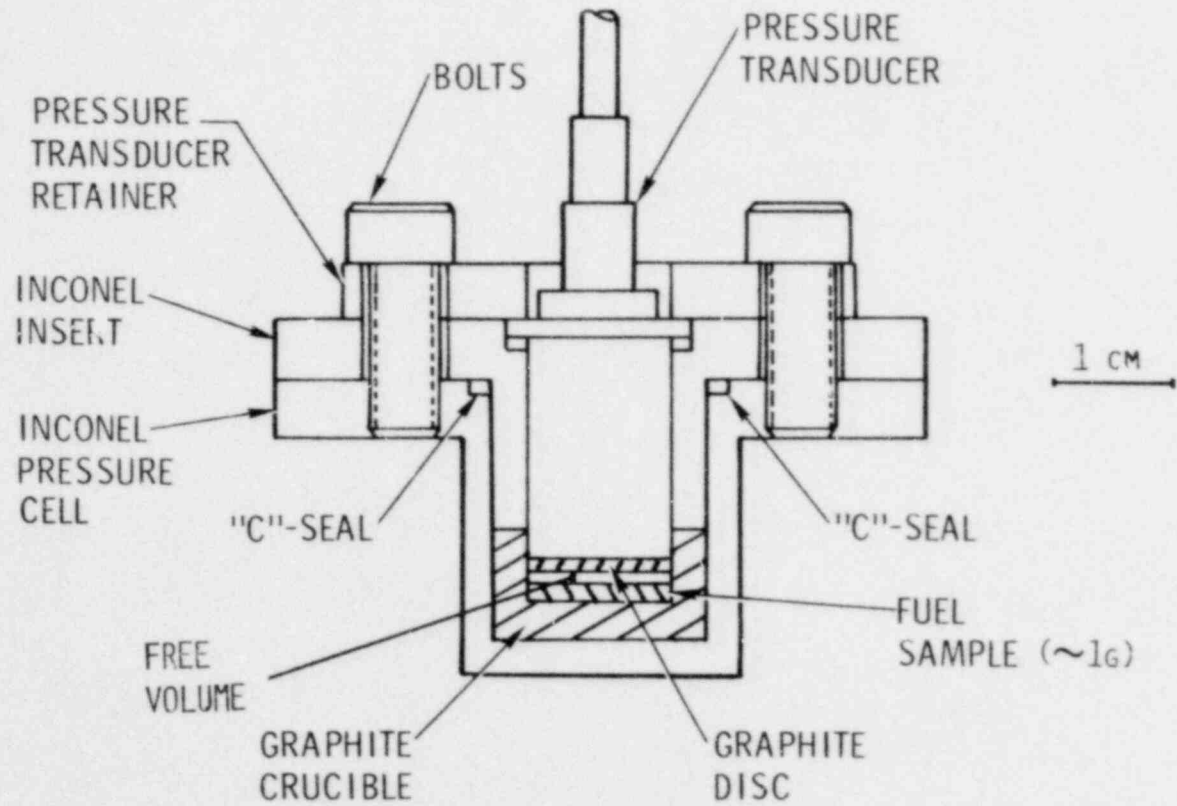


FIGURE 7. EOS PRESSURE CELL ASSEMBLY

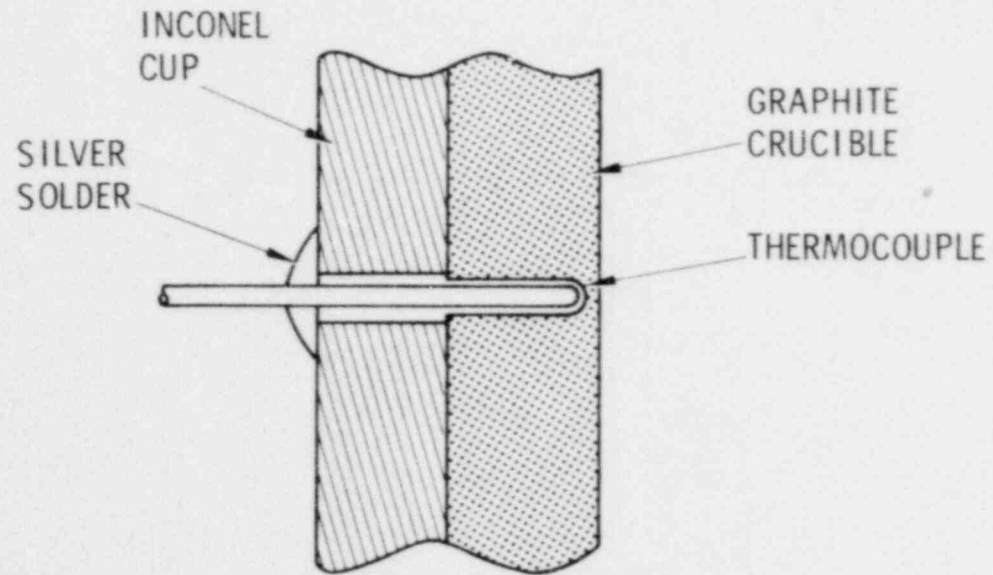


FIGURE 8. TYPICAL THERMOCOUPLE PENETRATION  
(Not to Scale)

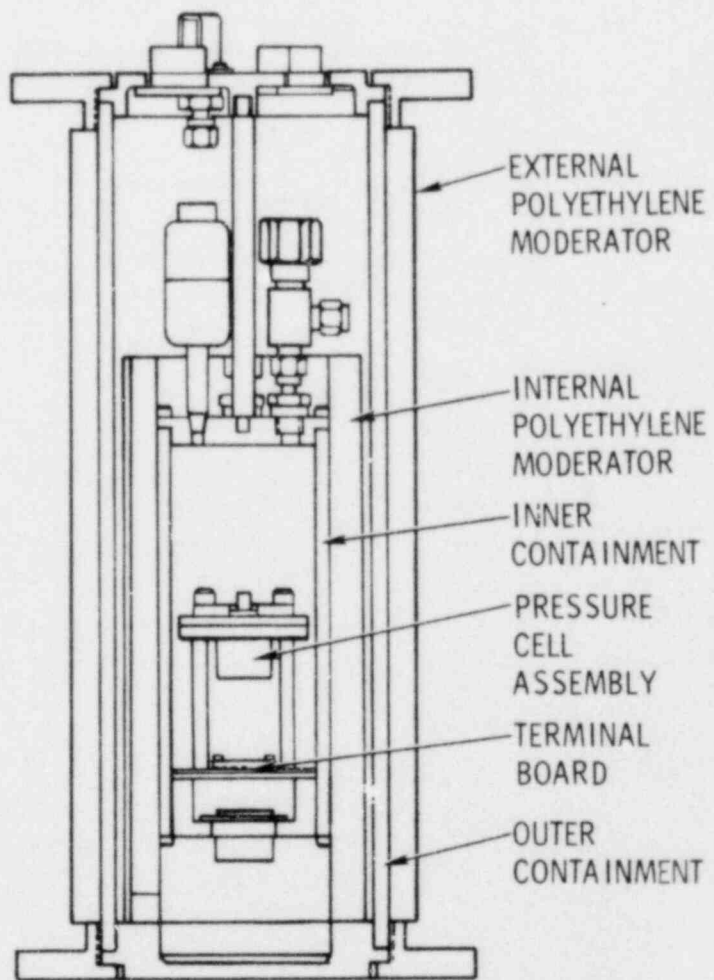


FIGURE 9. EEOS INPILE PACKAGE



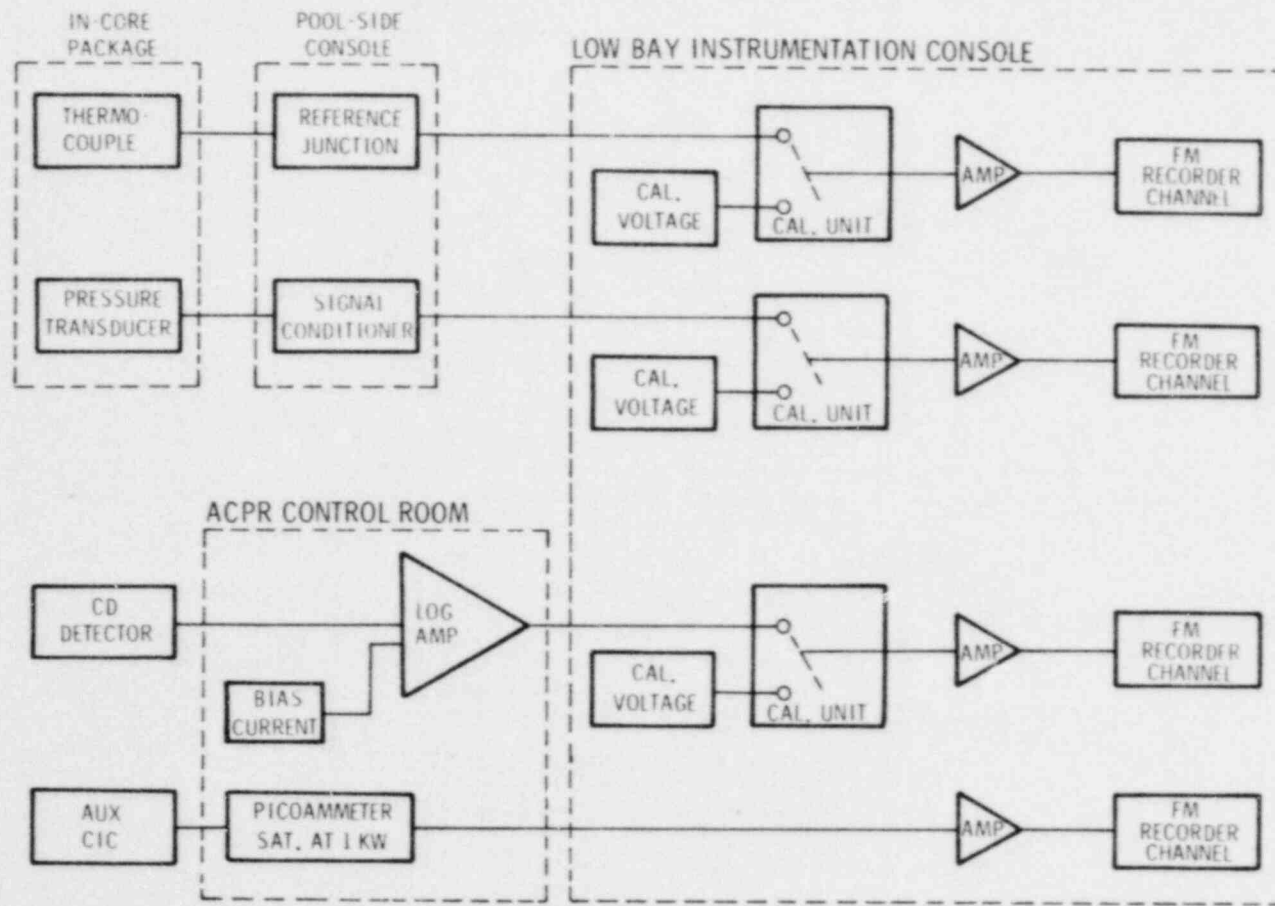


Figure 10. Block Diagram of Data Acquisition System

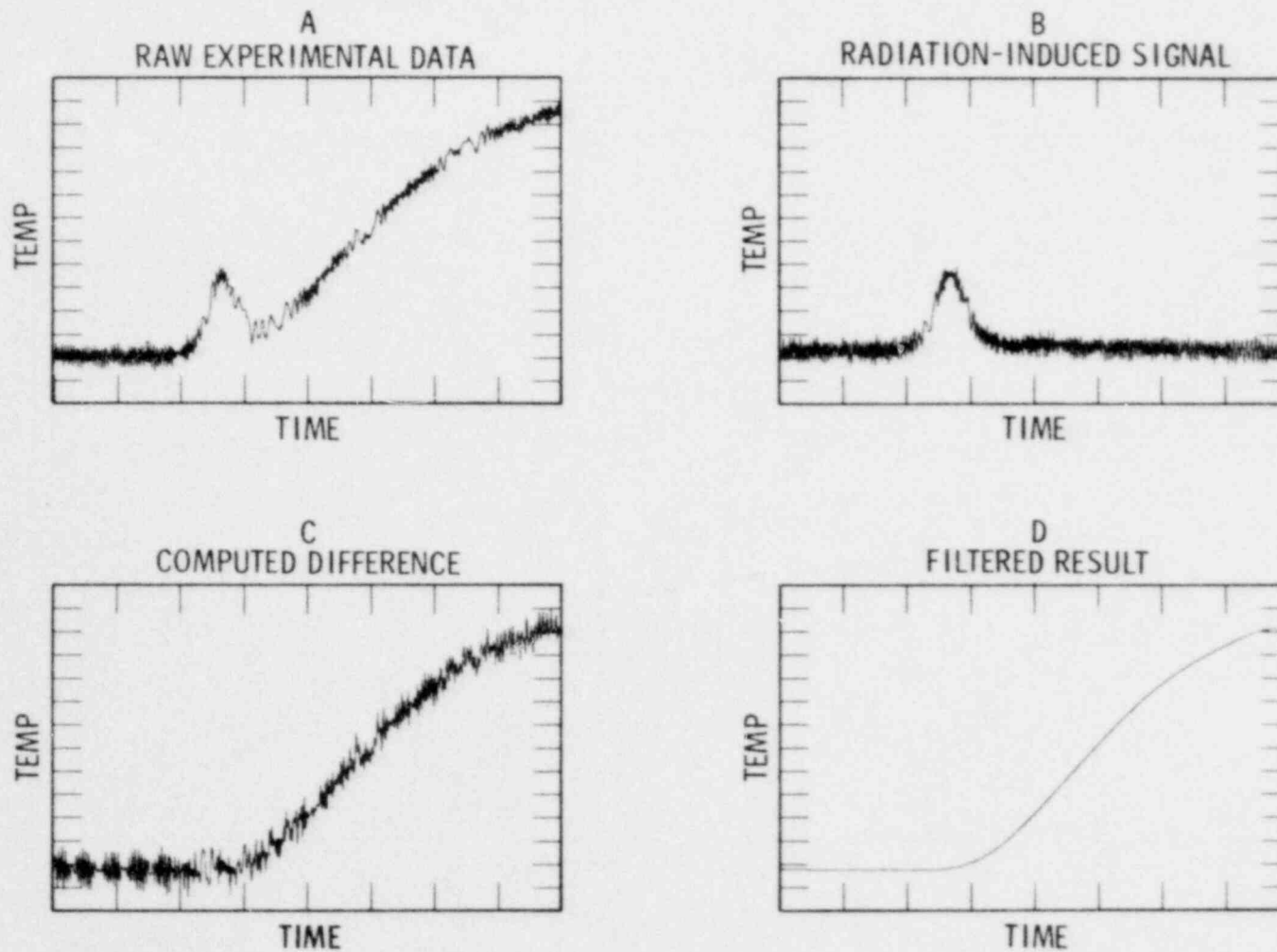


Figure 11. Results of Radiation Noise Correction and Filtering Techniques for Typical Thermocouple Data.

FIGURE 12A

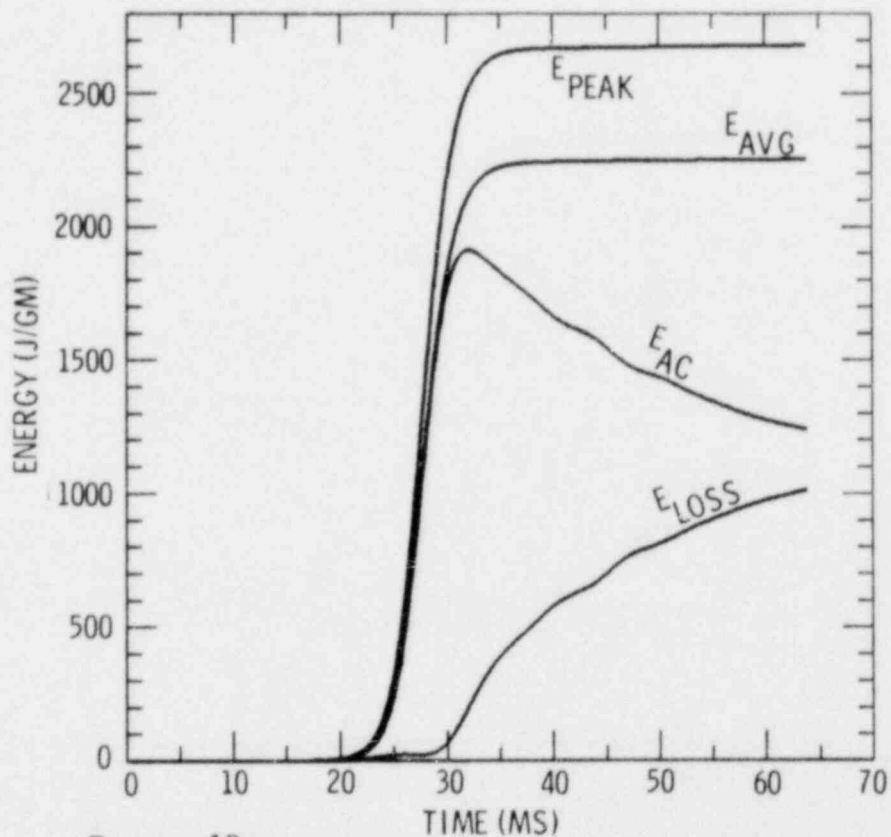


FIGURE 12B

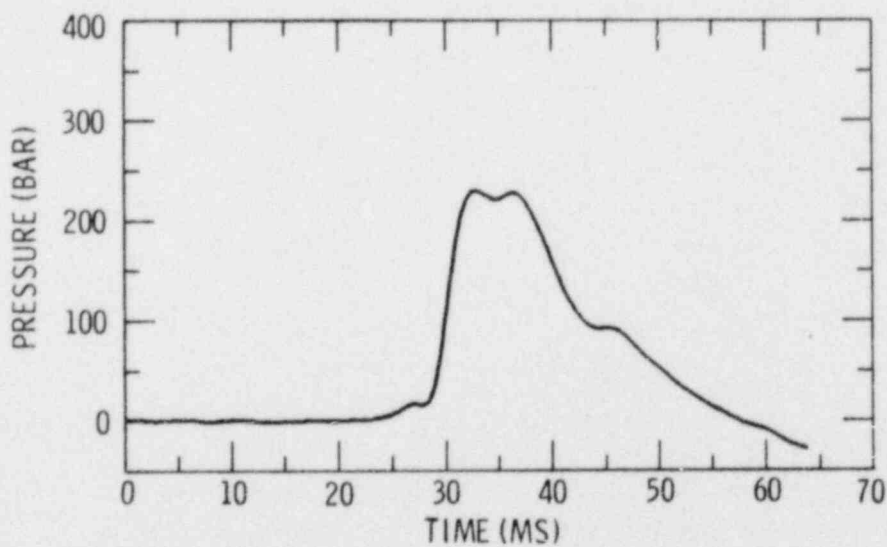


FIGURE 12. TYPICAL EEOS PRESSURE AND ENERGY HISTORIES

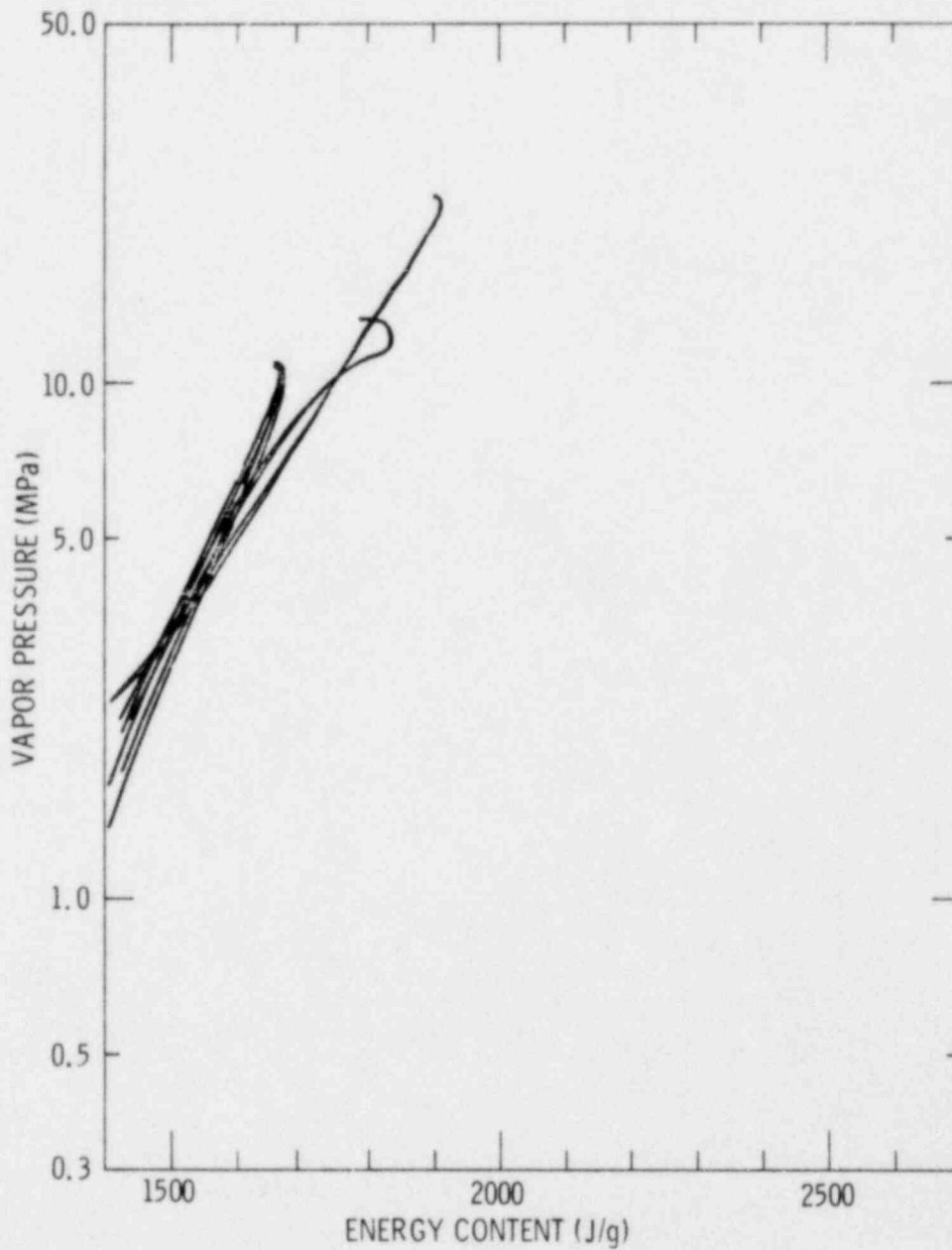


Figure 13. Pressure vs. Energy Relationships Using Pressure and Corrected Average Energy Data from Experiments EEOS-UO2-2,3,4.

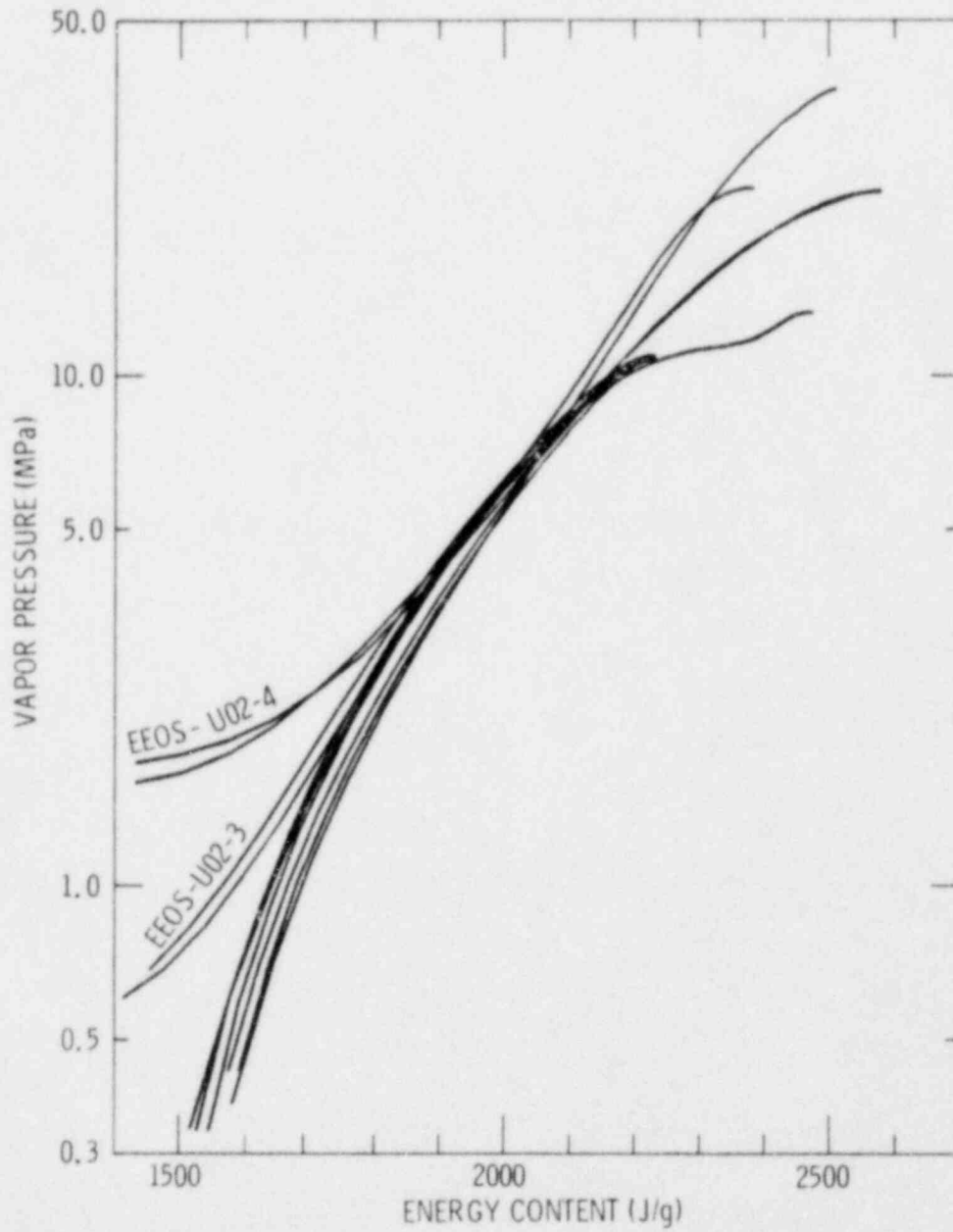


Figure 14. Pressure vs. Energy Relationships Using Pressure and Peak Energy Data from Experiments EEOS-UO2-1,2,3,4.

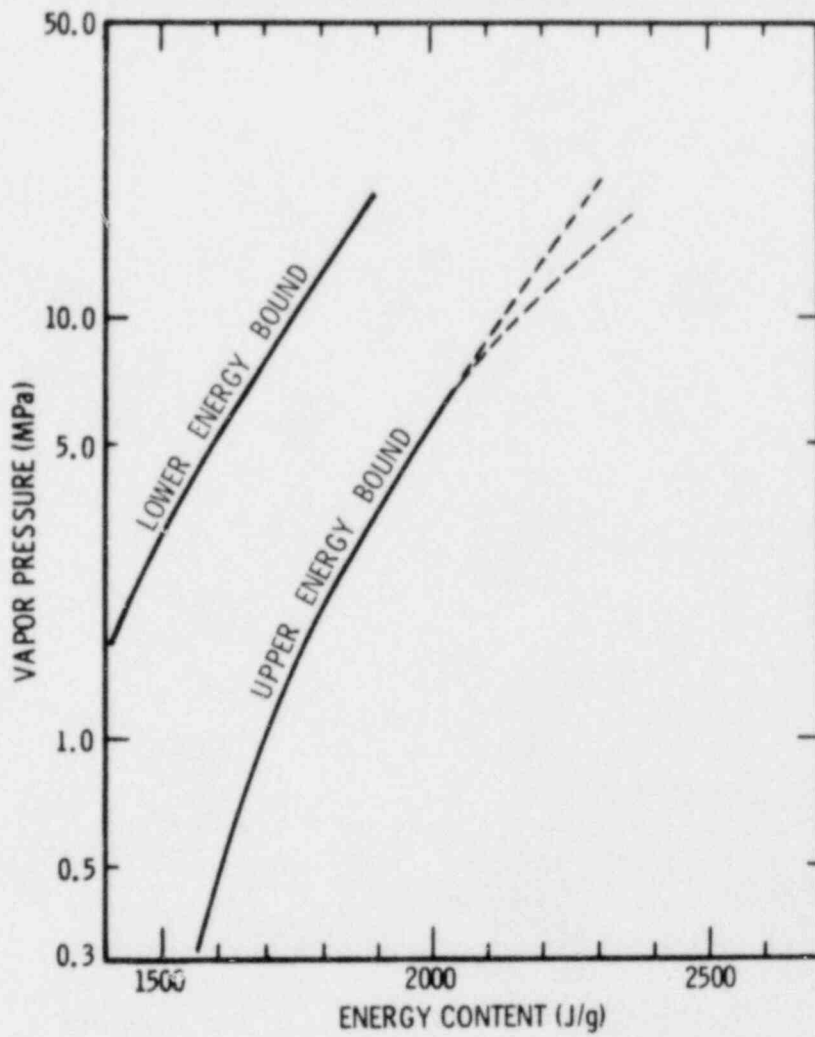


Figure 15. Upper and Lower Bounds on Vapor Pressure of  $\text{UO}_{2.08}$  Using Data from Figures 13 and 14.

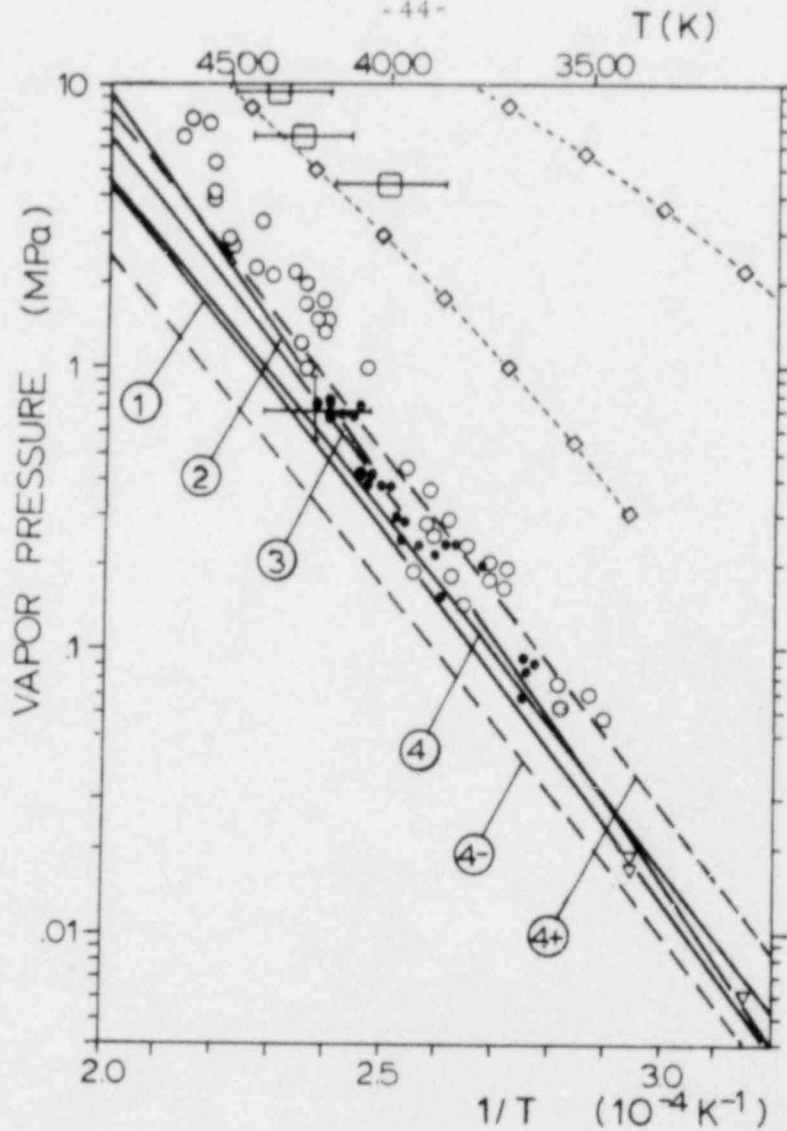


Figure 16. Vapor Pressure of  $UO_2$  as Function of Reciprocal Temperature.

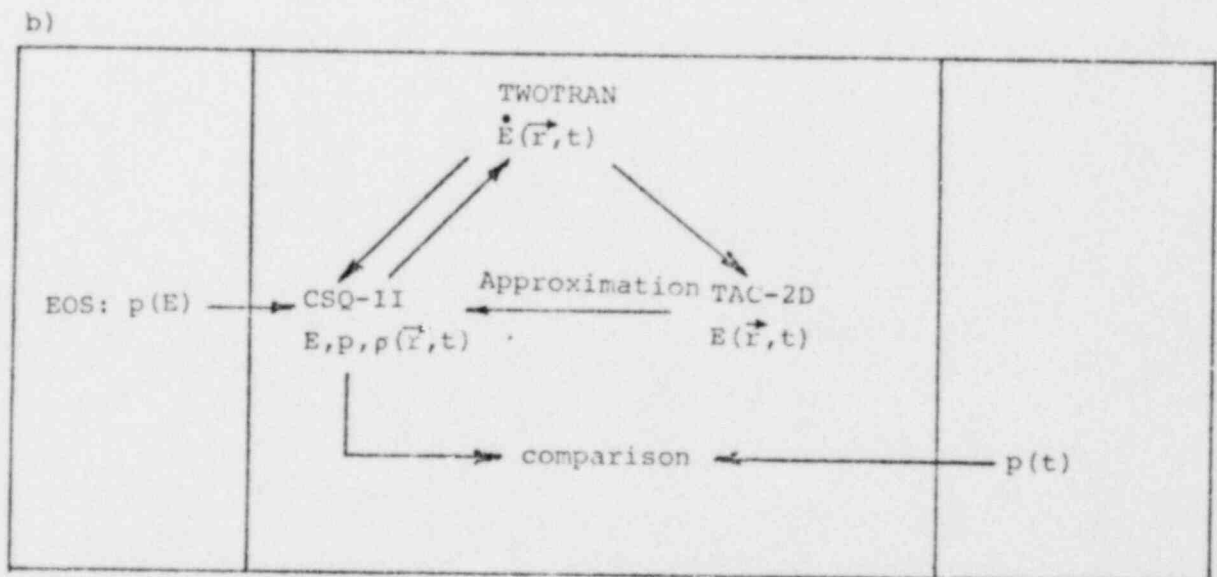
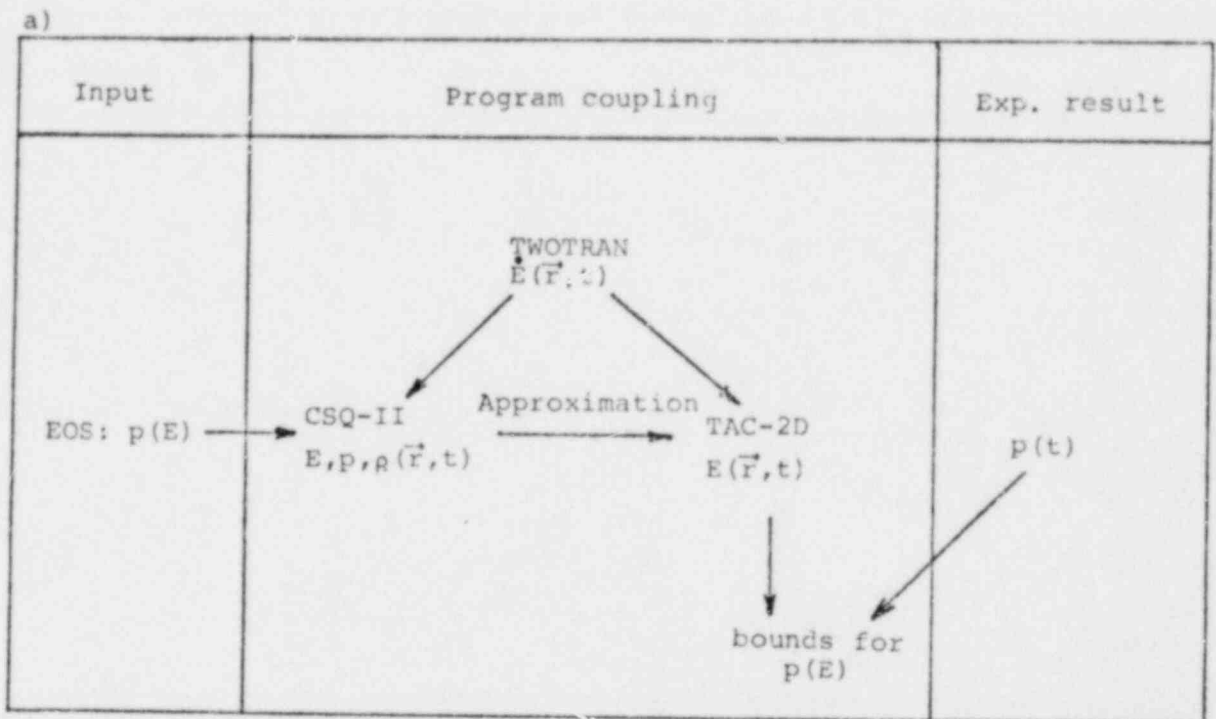
For references see Ref. 3 of this report.

I. Measurements:

- KfK, 1978 (2), laser evaporation
  - KfK, 1975 (3), laser evaporation
  - TUI, 1977 (4), laser evaporation
  - ANL, 1972 (5), transpiration method
  - SANDIA, 1977 (6), electron beam heating\*
  - SANDIA, 1977 (7), neutronic in-pile heating\*  
(upper and lower bound)
- \*In these experiments the vapor pressure was measured vs. enthalpy. For conversion to temperatures the following presently recommended relation was used:  
 $H(T) - H(298) = 1425. + (T - 3138) \cdot .504 \text{ J/g} \text{ (} T > 3138 \text{ K)}$

II. Calculations:

- (1) UKAEA, 1966 (8), Corresponding States
- (2) ANL, 1979 (9), modified Law of Mass Action
- (3) UKAEA, 1977 (10), Significant Liquid Structures
- (4) KfK, 1978 (2), Law of Mass Action
- (4+) 70% confidence interval, resulting from the present
- (4-) scatter in the input data of (4).



- $\dot{E}(\vec{r}, t)$     neutronic energy deposition
- $E(\vec{r}, t)$     fuel energy distribution
- $p(\vec{r}, t)$     pressure distribution
- $\rho(\vec{r}, t)$     fuel density distribution

Figure 17. Coupling of two-dimensional codes for neutronics (TWOTRAN), hydrodynamics (CSQ-II) and heat transfer (TAC-2D) as used in the analysis of EOS experiments on  $UO_2$ .



FIGURE 18. HYDRODYNAMICS

- 2-DIMENSIONAL HYDRODYNAMIC CODE CSQ WAS USED
- CSQ ASSUMES INSTANTANEOUS PRESSURIZATION (NOT NUCLEATION SITE LIMITED)
- SPACE FIXED, TIME INDEPENDENT ENERGY DEPOSITION GRID
- RESULTS:
  - MOTION DUE TO FUEL VAPORIZATION ONLY
  - EARLY DISPERSAL DURING PRESSURIZATION TIME
  - BUT FUEL IS DRIVEN OUT OF HIGH ENERGY REGIONS
  - SO DISPERSAL IS UNDERESTIMATED BY CURRENT CSQ-VERSION,  
IMPROVEMENT OF NEUTRONIC-HYDRODYNAMIC COUPLING REQUIRED

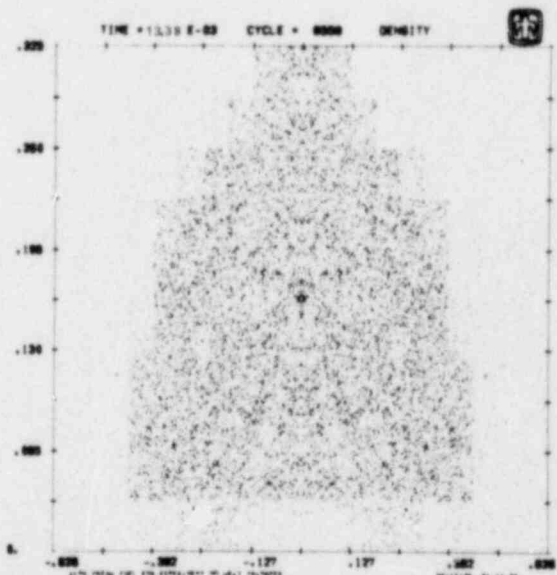
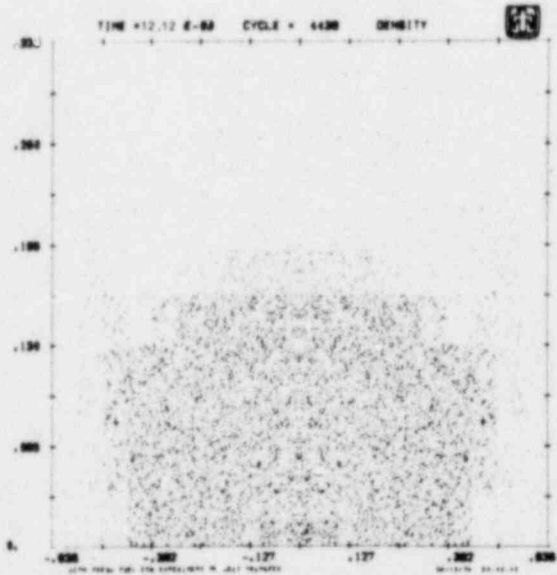
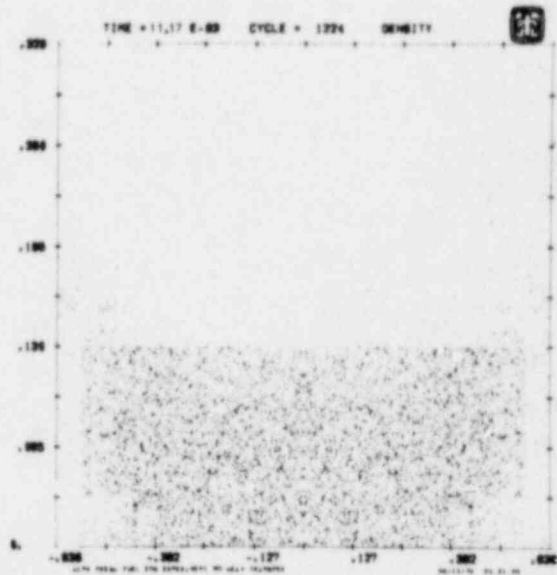
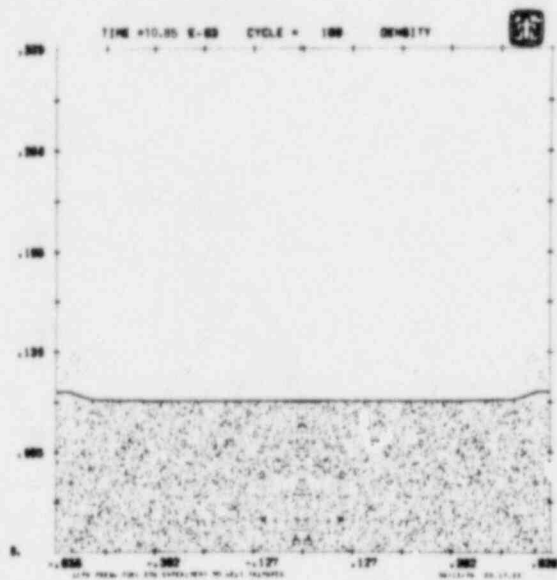
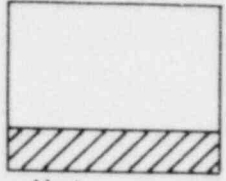
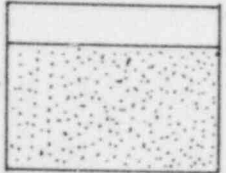
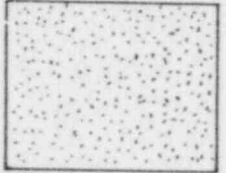
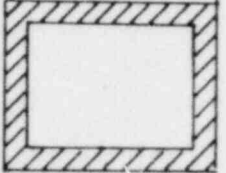


Figure 19. Fuel motion in the container volume as calculated with the hydrodynamic code CSQ-II. Time of peak power is 10.00 msec.

FIGURE 20.    NEUTRONICS

- \* 2-DIMENSIONAL NEUTRON TRANSPORT CODE TWOTRAN WAS USED
  
- \* CALCULATIONS FOR DIFFERENT FUEL GEOMETRIES WHICH ARE EXPECTED TO OCCUR DURING THE COURSE OF THE EXPERIMENT
  
- \* RESULTS: AVERAGE AND PEAK FUEL ENTHALPIES TAKING INTO ACCOUNT GEOMETRY CHANGES AFTER FUEL MELTING

FIGURE 21. RESULTS OF NEUTRONIC ENERGY DEPOSITION CALCULATIONS FOR DIFFERENT FUEL GEOMETRIES

FUEL GEOMETRY	PEAK TO AVERAGE RATIO	PEAK TO MINIMUM RATIO	RELATIVE TOTAL ENERGY INPUT	
DISK	1.34	1.53	100%	 disk
75% SMEARED	1.25	1.49	107%	 75% smeared
100% SMEARED	1.24	1.48	112%	 100% smeared
SHELL	1.17	1.24	117%	 shell

-49-

FIGURE 22. HEAT TRANSFER

- \* MODIFIED 2-DIMENSIONAL HEAT CONDUCTION CODE TAC2D WAS USED TO CALCULATE FUEL ENTHALPIES
- \* HEAT TRANSFER MECHANISMS TREATED:
  - CONDUCTION WITHIN FUEL
  - CONDUCTION TO CONTAINER
  - RADIATION TO CONTAINER (1-DIM.)
  - HEAT OF FUSION
  - HEAT OF EVAPORATION
- \* STEPWISE CHANGE OF FUEL GEOMETRY WHEN COLDEST NODE PASSED MELTING TEMPERATURE. GEOMETRY CHANGES CONSIDERED:
  - DISK TO 100% SMEARED GEOMETRY
  - DISK TO SHELL GEOMETRY
- \* COMPLETE THERMAL MIXING UPON DISPERSAL
- \* NO OR TOTAL THERMAL MIXING AT LATER TIMES
  - LOWER AND UPPER BOUNDS FOR FUEL ENTHALPY
- \* ENERGY DEPOSITIONS FOR THE DIFFERENT FUEL GEOMETRIES AS CALCULATED WITH TWOTRAN

THERMAL ANALYSIS OF EXPERIMENT EOS-UO2-4

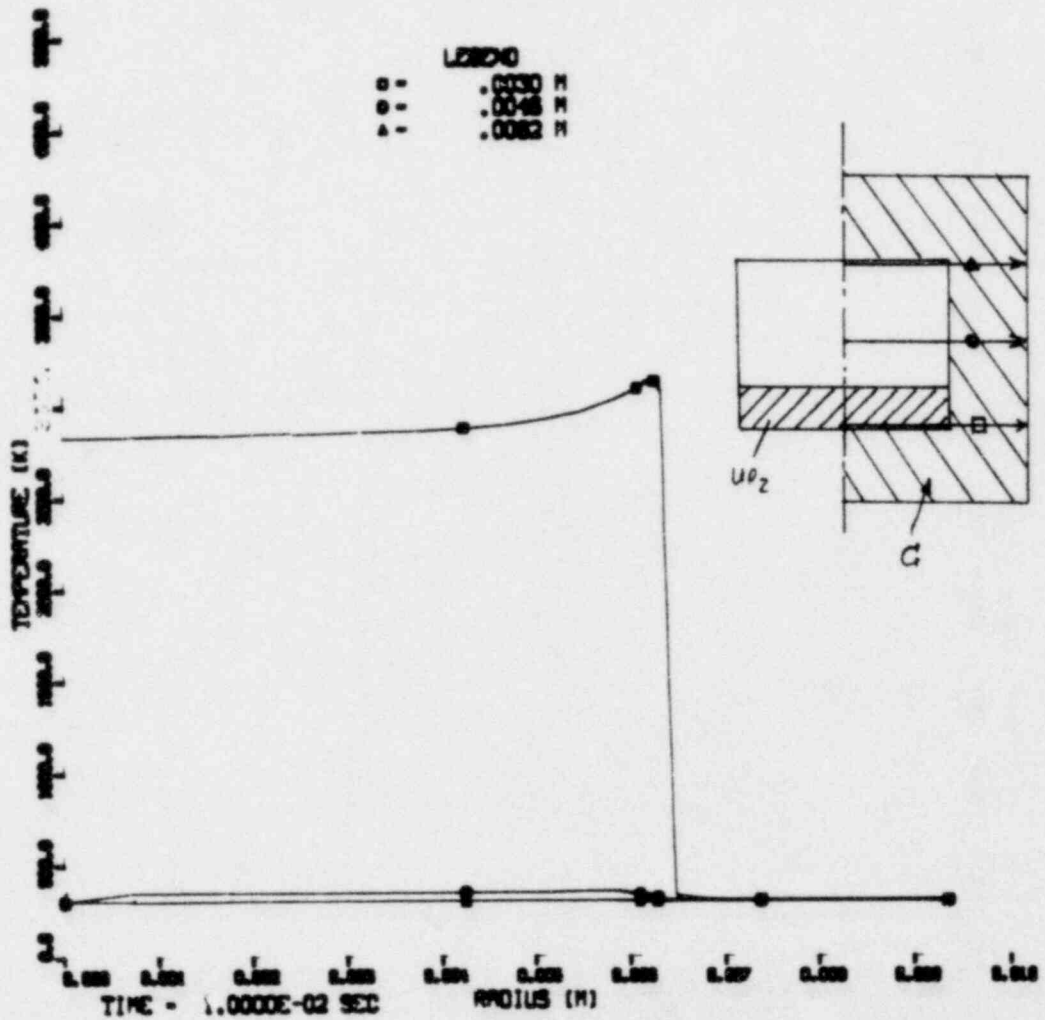


Figure 23. Calculated radial temperature distribution in the EEOS capsule at time of peak power for three axial positions (□ = bottom of fuel disk). Fuel is in the initial disk geometry.

THERMAL ANALYSIS OF EXPERIMENT EOS-UO2-4

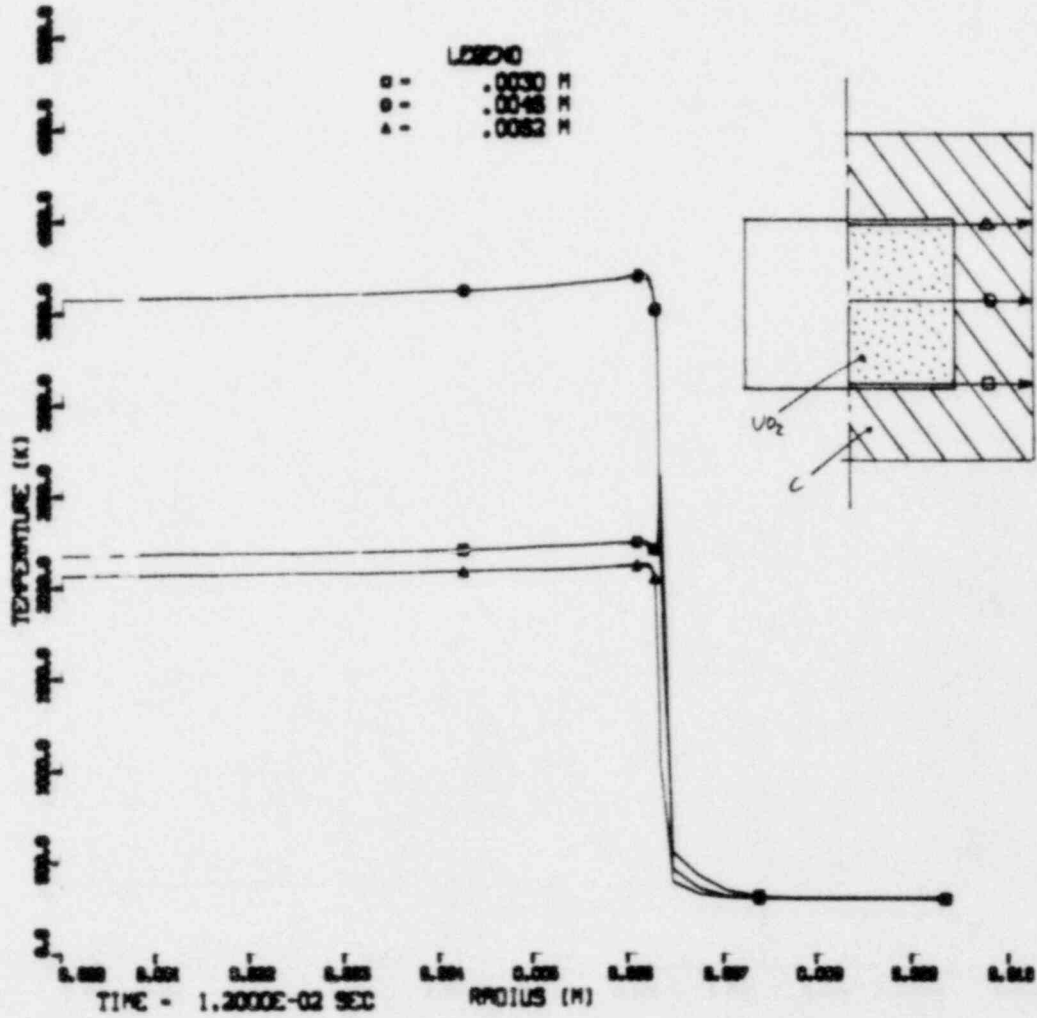


Figure 24. Calculated radial temperature distribution in the EOS capsule after fuel dispersal (center plane, upper and lower capsule surface).

Figure 25. Calculations for the Upper Limit of Fuel Enthalpies

Experiment	Average Energy Deposition	Geometry Transition	Modelling Assumptions	Curve Number
EEOS-UO <sub>2</sub> -2	1948 J/g	disk → shell disk → 100% smeared	1. complete thermal mixing at dispersal 2. no mixing at later times 3. heat for fuel vaporization taken from <u>total</u> fuel mass 4. <u>hottest</u> node was correlated to measured pressure	1
				2
EEOS-UO <sub>2</sub> -4	2257 J/g	disk → shell disk → 100% smeared		3
				4

A lower bound for the fuel enthalpies was calculated by

--including thermal mixing also at later times and by

-- correlating the calculated minimum temperatures of the inner shell surface to the measured pressures. The result is line 5 in Figure 6.



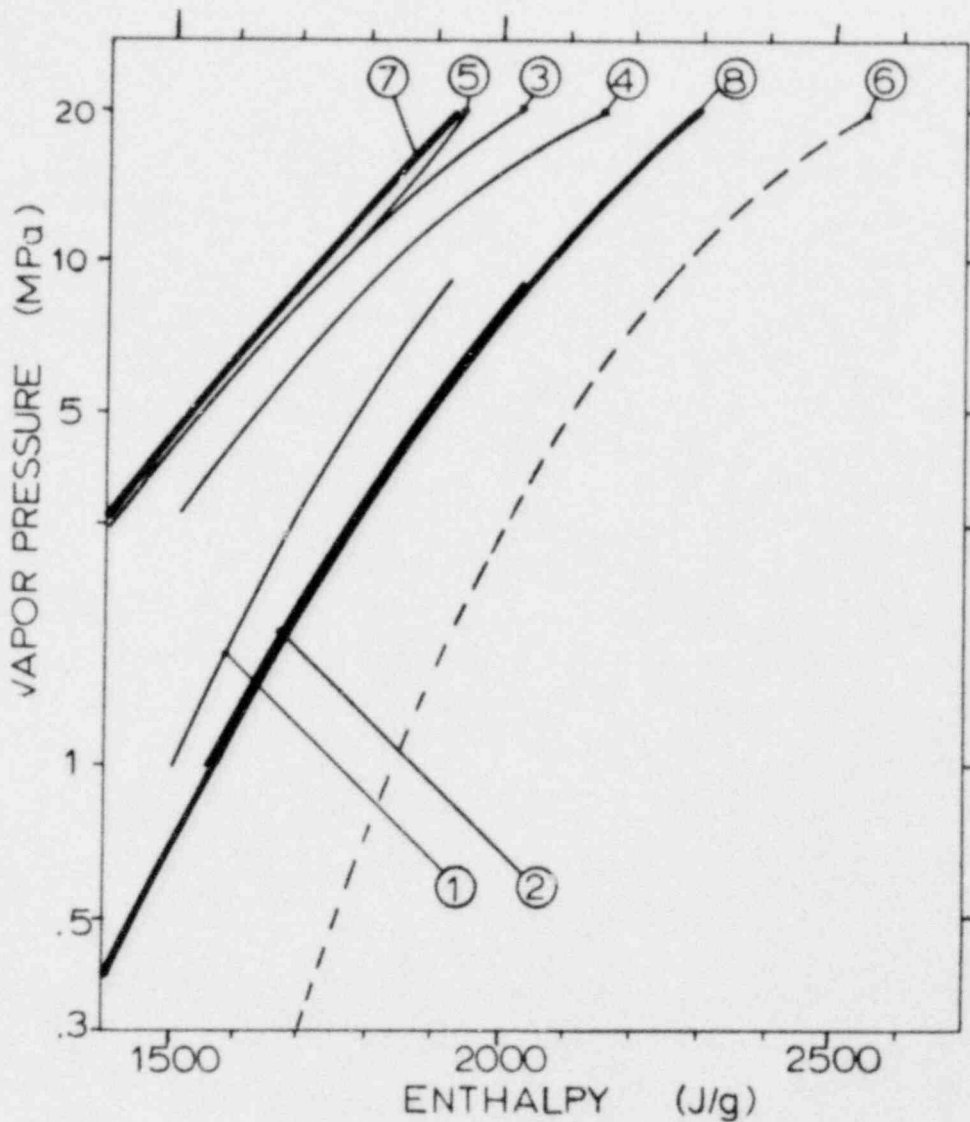


Figure 26. Vapor pressure-enthalpy relations as calculated from the experimental raw data:

- ① to ④ upper bounds for different experiments and model assumptions (see Table II) starting from peak enthalpy (curve 6)
- ⑤ calculated lower bound, starting from peak enthalpy (curve 6)
- ⑥ vapor pressure vs. peak enthalpy
- ⑦ and ⑧ lower and upper bounds for the effective  $UO_2$  enthalpy as resulting from the analysis.

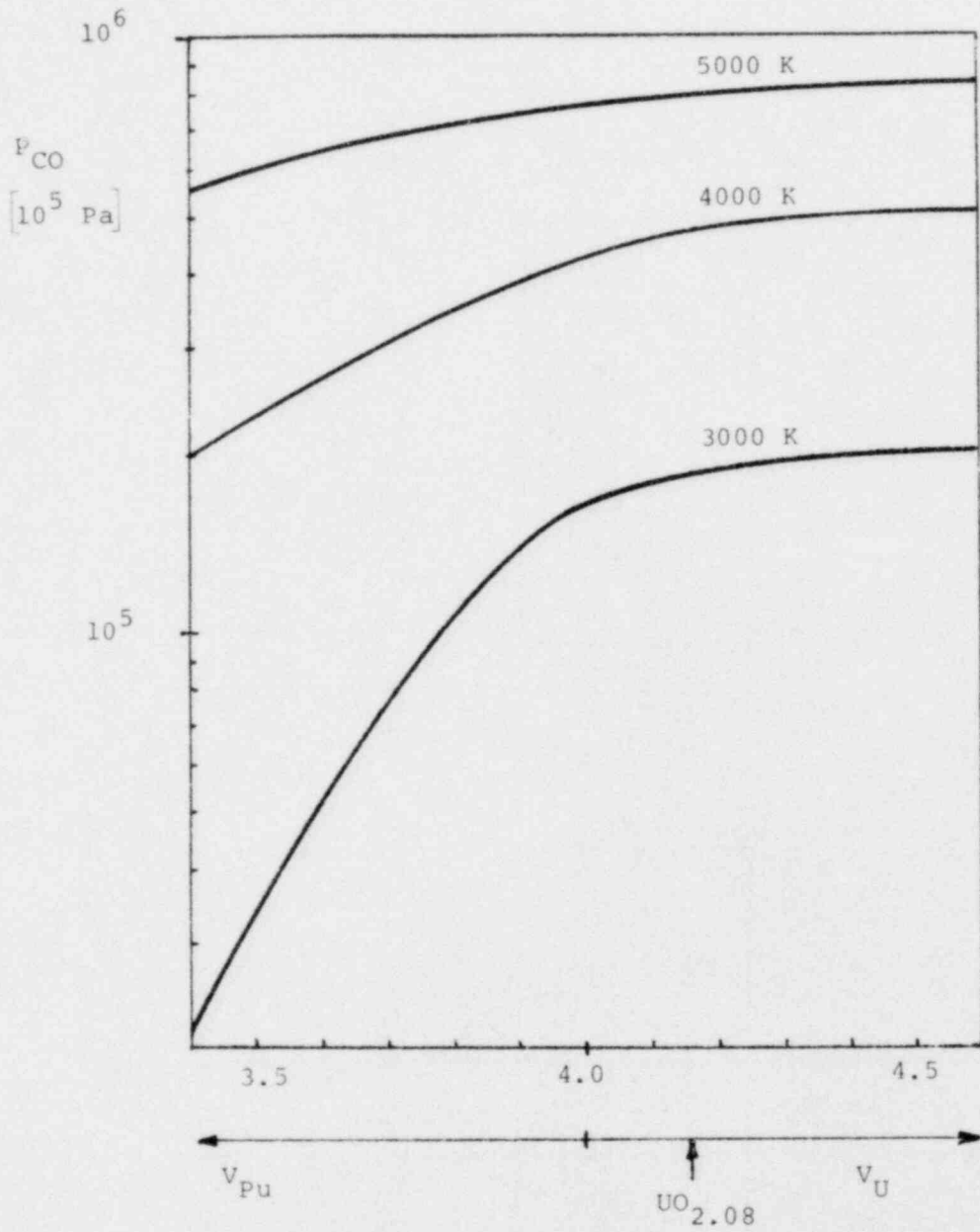


Figure 27. Calculated CO equilibrium pressures as function of plutonium and uranium valency. The EEOS experiments used  $UO_{2.08}$ .

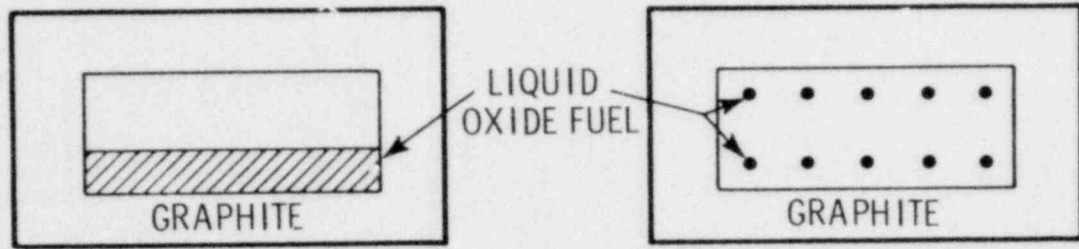


FIGURE 28A. SLAB GEOMETRY

FIGURE 28B. DROPLET GEOMETRY

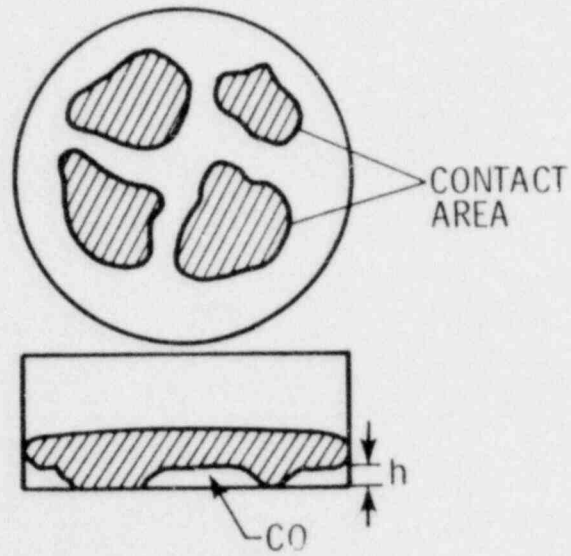


FIGURE 29. CO FILM FORMED AS OXYGEN DIFFUSION PROCEEDS

Figure 30. Summary of the Investigated Oxygen Diffusion Problems

geometrical configuration of liquid fuel	oxygen diffusion path	diffusion atmosphere	temperature (K)	curve number in Fig.31.	
slab geometry (Fig.28a)	diffusion via gas phase	UO <sub>2</sub> vapor (fresh fuel)	3000	1	
			4000	2	
			5000	3	
		Xe-UO <sub>2</sub> mixture (irr. fuel)	4000	4	
			5000	5	
	fuel-graphite interface undisturbed	diffusion out of liquid oxide fuel to graphite surface	---	bulk fuel 5000 fuel/graphite interface 3380	6
	spreading and collapsing CO-film (Fig. 29)		---	bulk fuel 5000 fuel/graphite interface 3380	7
droplet geometry (Fig.28b)	diffusion via gas phase	UO <sub>2</sub> vapor	3000	8	
			4000	9	
			5000	10	
		Xe-UO <sub>2</sub> vapor	3000	11	
			4000	12	
			5000	13	
	diffusion via gas phase	UO <sub>2</sub> vapor	3000	14	
			4000	15	
			5000	16	
Xe-UO <sub>2</sub> vapor	3000	too small			
	4000	17			
5000	18				

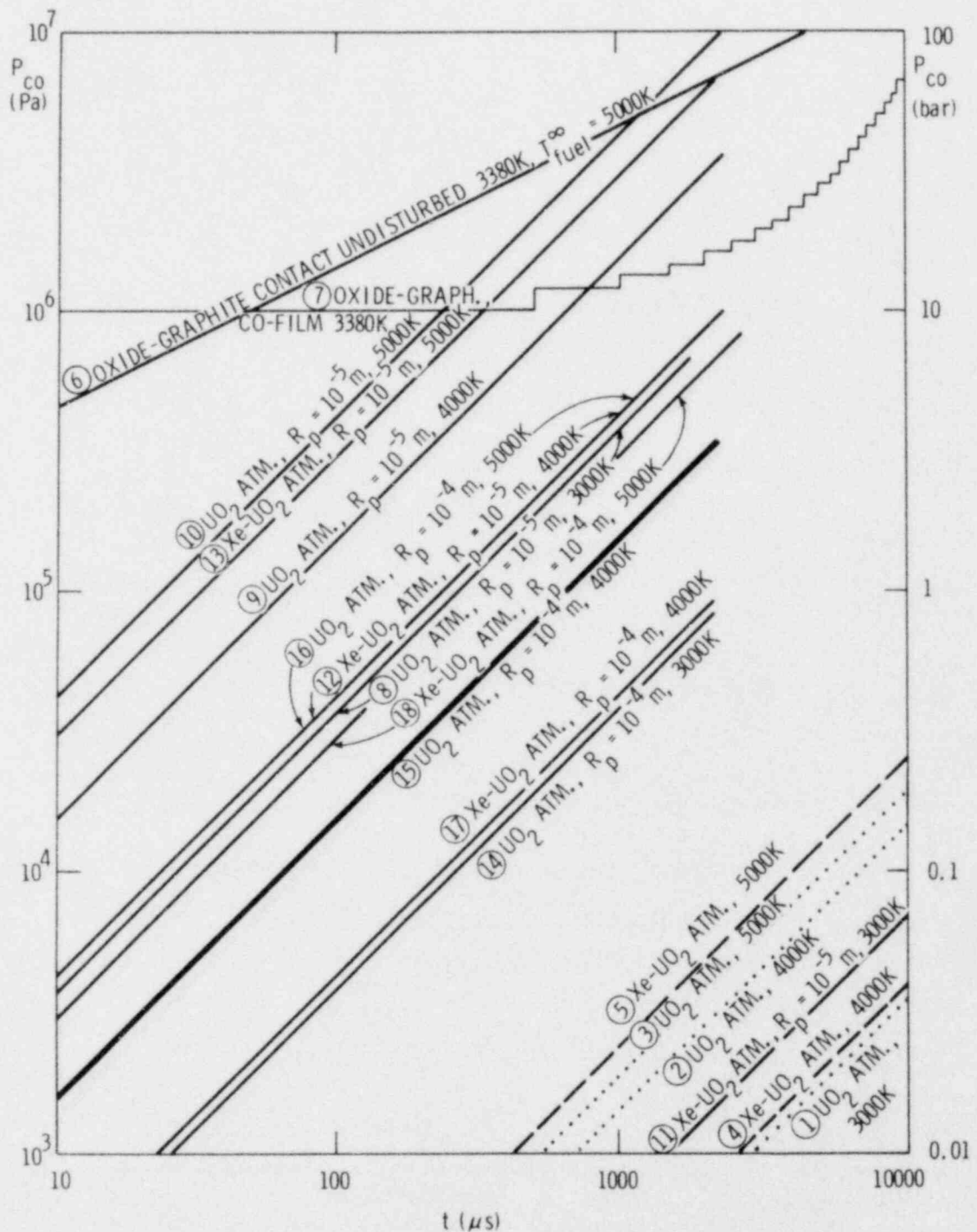


FIGURE 31. CALCULATED MAXIMUM CO-PARTIAL PRESSURES VS. TIME FOR DIFFERENT CAPSULE CONDITIONS AND FUEL GEOMETRIES. RESULTS FROM CSQ, TAC-2D AND PIE-WORK LEAVE CO-FORMATION ACCORDING TO CURVE 15 AS THE HIGHEST POSSIBLE CO-PRESSURE GENERATION. ADDITIONAL INHIBITING PROCESSES, LIKE LIMITED C-O-REACTION KINETICS AND A VAPOR DEPOSITED FUEL LINER, ASSURE NEGLIGIBLE CO-FORMATION DURING THE EEOS EXPERIMENTS.

FIGURE 32. RECOMMENDATIONS FOR ACRR EOS EXPERIMENTS

EXPERIMENT DESIGN

1. OBTAIN FLATTEST DEPOSITION PROFILE POSSIBLE
  - MINIMIZES HYDRODYNAMIC MOVEMENT
  - MINIMIZES PRESSURE GRADIENTS IN SAMPLE
  - MINIMIZES ENERGY DEPOSITION CHANGES WITH MOVEMENT
  - MINIMIZES INITIAL TEMPERATURE GRADIENT
2. USE POWDER, SMALL FREE VOLUME (50%)
  - FLATTER ENERGY DEPOSITION PROFILE
  - SMALL MIXING LENGTH
  - LOW EFFECTIVE CONDUCTIVITY (LESS HEAT LOSS)
3. USE OXIDE LINER (LOWER ENRICHMENT THAN SAMPLE)
  - NO CHEMICAL REACTIONS
  - NEAR ADIABATIC CONDITIONS
  - NO ANOMALOUS VAPOR PRESSURES
4. ELIMINATE IMPURITIES FROM HANDLING

POOR ORIGINAL

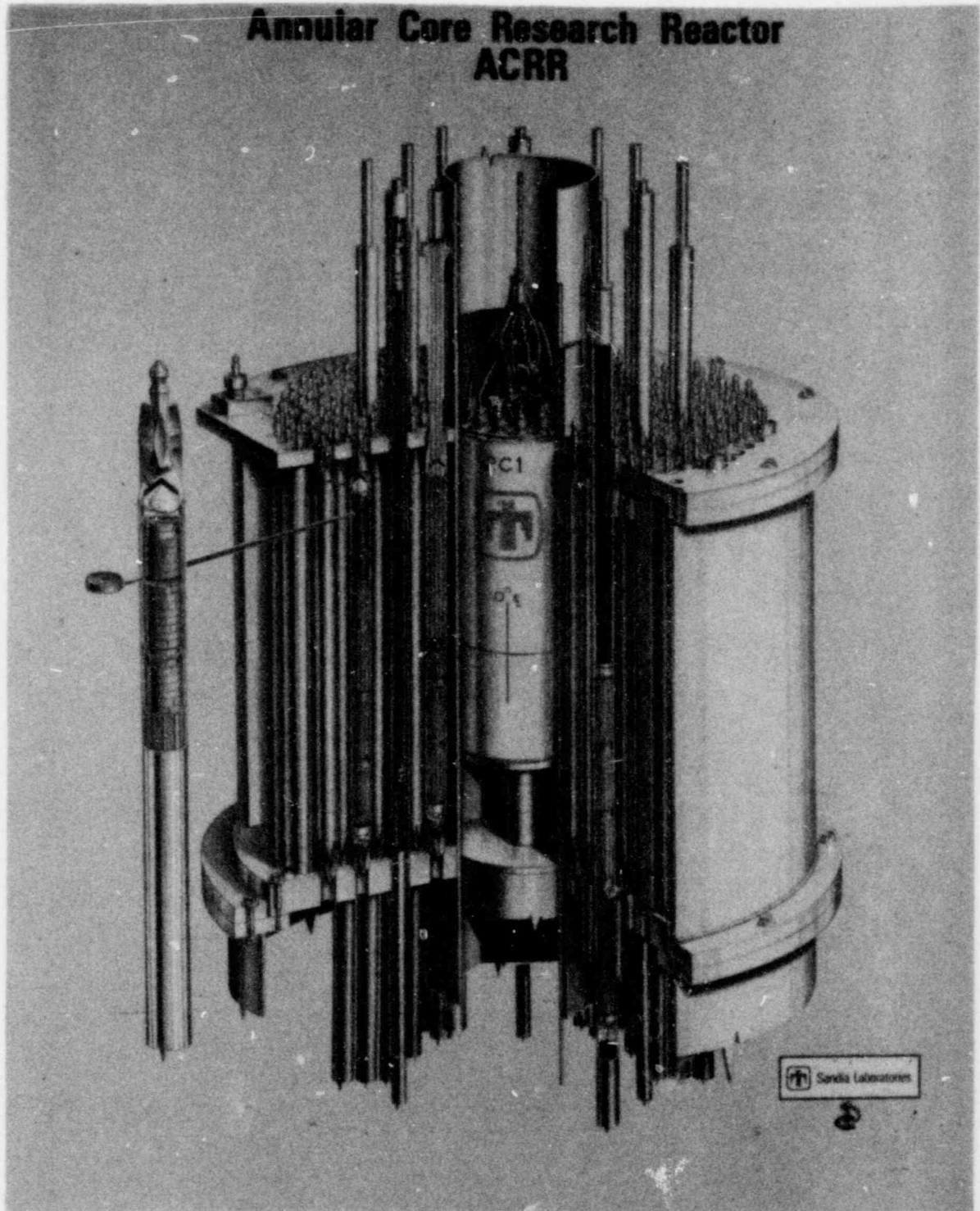


Figure 33. Core configuration of the ACRR



FIGURE 34. OPERATIONAL CHARACTERISTICS OF THE ACRR

PULSE OPERATIONS

REACTIVITY INSERTION	\$2.95
PEAK POWER	29,500 MW
PULSE WIDTH (FWHM)	6.5 MSEC
REACTOR PERIOD	1.65 MSEC
ENERGY RELEASE	350 MJ
NEUTRON FLUENCE	$7.4 \times 10^{15}$ N/CM <sup>2</sup>
PEAK NEUTRON FLUX	$6.1 \times 10^{17}$ N/CM <sup>2</sup> -SEC
GAMMA DOSE	2.9 MRAD
PEAK GAMMA DOSE RATE	240 MRAD/SEC
FUEL TEMPERATURE - $\Delta T$	1050°C

STEADY-STATE OPERATIONS

POWER	2 MW(TH)
NEUTRON FLUX	$4.2 \times 10^{13}$ N/CM <sup>2</sup> -SEC
GAMMA DOSE RATE	$1.6 \times 10^4$ RAD/SEC
FUEL TEMPERATURE	960°C

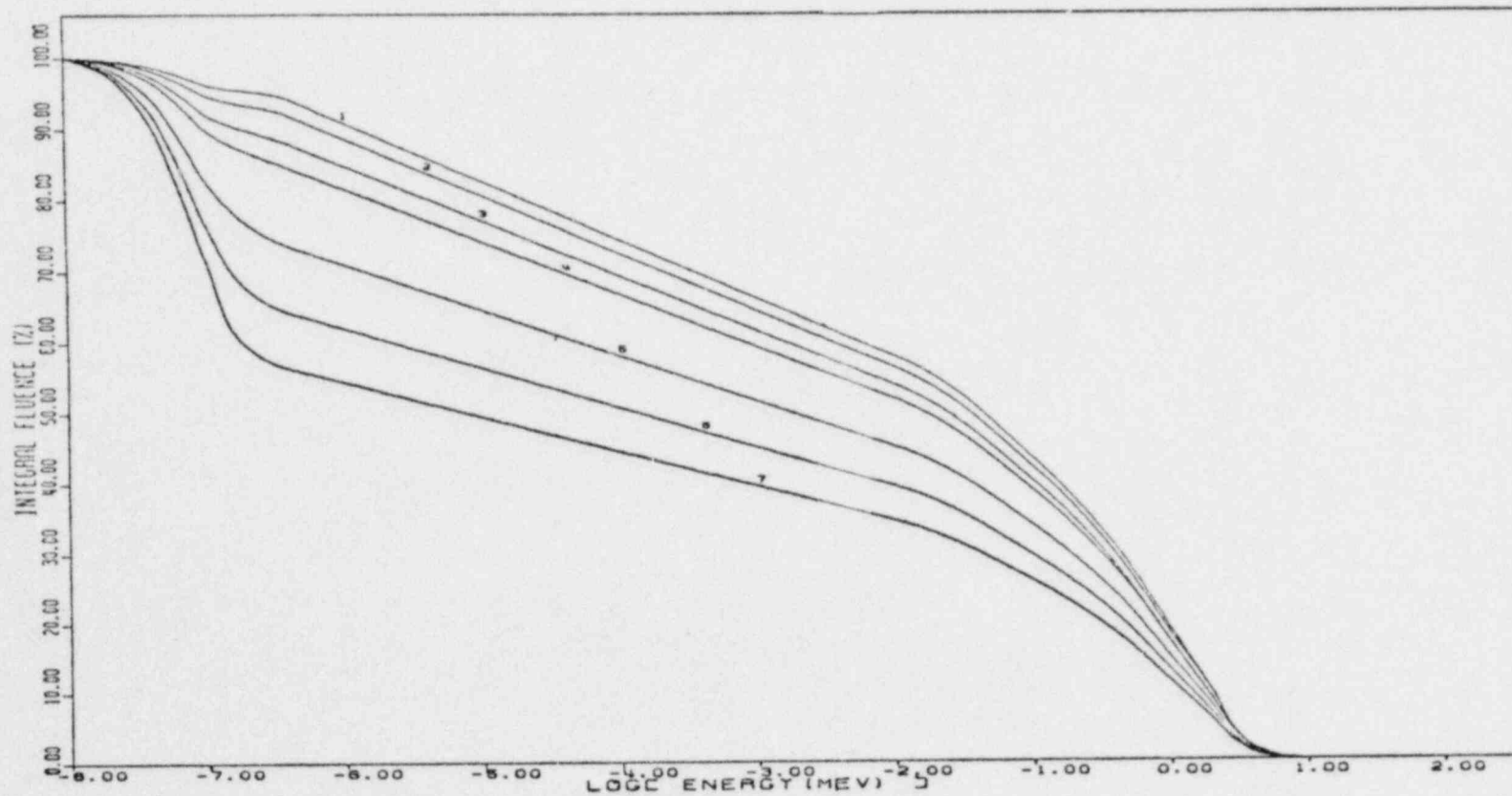


Figure 35. Integral neutron spectra for ACRR: 1., 2., and 3. free field measurements at center, bottom, and top of experimental cavity ; 4., 5., 6., and 7. center of the experimental cavity with polyethylene moderation thicknesses of 0.635 cm, 1.270 cm, 1.905 cm, and 2.540 cm .

Figure 36. ACRR SINGLE AND MULTI-PIN SLOTTED CORE CAPABILITIES

(Preliminary Calculations)

Suggested Configuration to Achieve 3000 J/g

	Fuel Enrichment	Poly Thickness (inch)	Released Reactor Energy (MJ)	Energy Deposited in Test Pin (J/g)
Single Pin	12%	1/4"	300	3000
	12%	3/4"	175	3000
Seven Pin	40/30% (31%)	3/4"	220	3400
19 Pin	60/35/20 (22%)	3/4"	300	>3600

Maximum Energy Deposition

Single Pin	20%	3/4"	300	6850
	93%	3/4"	300	16000
Seven Pin	20%	3/4"	300	3700
	93%	3/4"	300	8500
19 Pin	20%	3/4"	300	>2800
	93%	3/4"	300	>6800

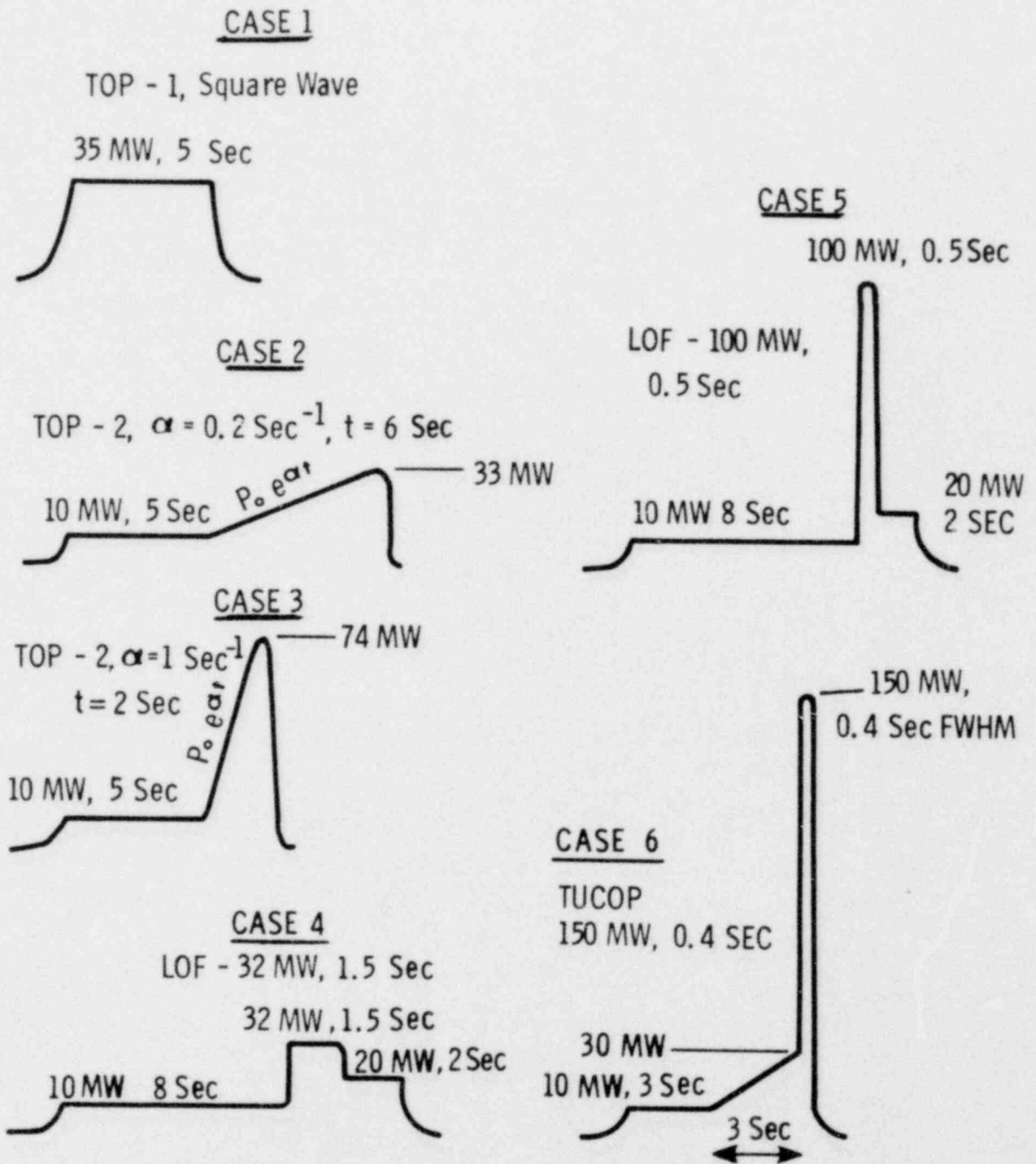


Figure 37. Advanced operational modes possible in the ACRR. The numbers shown are preliminary and subject to further changes due to hardware improvements, like higher worth control rods and fully programmable rod movements.

FIGURE 38. ACPR/ACRR PERFORMANCE CHARACTERISTICS

	ANNULAR CORE PULSE REACTOR (ACPR)	ANNULAR CORE RESEARCH REACTOR (ACRR)
FUEL TEMPERATURES SAFETY LIMIT PEAK FUEL TEMPERATURE	930°C/1000°C 870°C	1800°C 1100°C (1350°C)
STEADY-STATE OPERATION MAXIMUM POWER NEUTRON FLUX (>10 KEV)	600 kW $6.1 \times 10^{11}$ N/CM <sup>2</sup> /SEC	2.0 MW $2.2 \times 10^{12}$ N/CM <sup>2</sup> /SEC
PULSE OPERATION REACTIVITY PEAK POWER ENERGY RELEASE NEUTRON FLUENCE (>10 KEV) PULSE WIDTH (FWHM) TEMPERATURE COEFFICIENT	\$4.50 15,000 MW 108 MJ $1.1 \times 10^{15}$ N/CM <sup>2</sup> 4.5 MSEC -1.2¢/°C	\$2.95 (\$3.50) 30,000 MW (52,000 MW) 360 MJ (450 MJ) $4.0 \times 10^{15}$ N/CM <sup>2</sup> ( $4.9 \times 10^{15}$ N/CM) 6.7 MSEC (5.3 MSEC) -0.65¢/°C

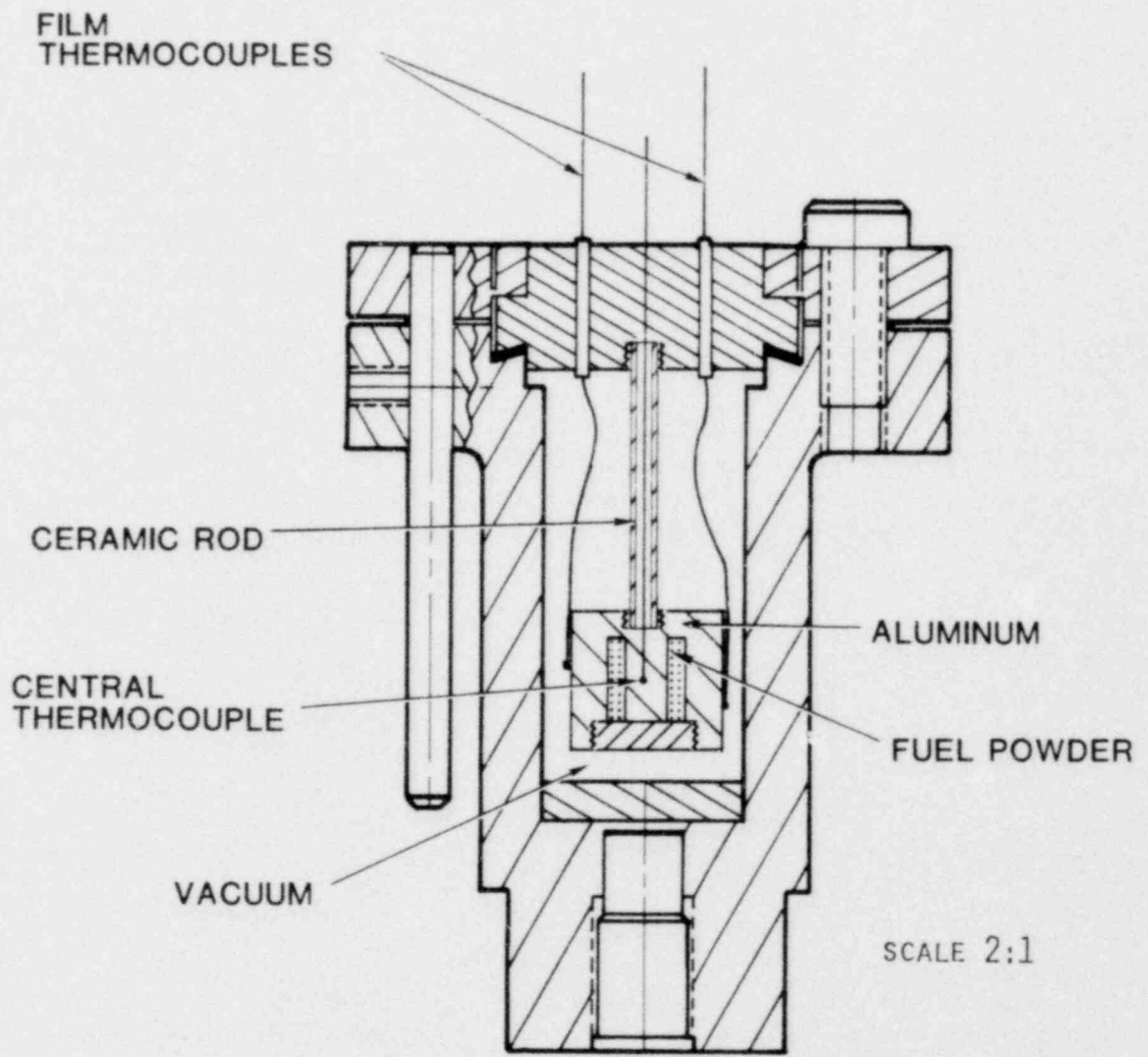


Figure 39. Cross-section of In-Pile Calorimeter

Figure 40. Preliminary Design of In-Pile Calorimeter

1. Calorimeter body

- cylinder from high strength aluminum (ultimate tensile strength 400 MPa)
- aluminum mass 4.6 g
- outer surface polished
- vacuum environment ( $<10^{-5}$  Torr)
- fuel mass 1 g
- energy deposition 1500 to 2500 J
- calorimeter temperature increase 300 to 500 K
- stresses for 80 MPa fuel vapor pressure  $<240$  MPa
- radius increase of Al body under 80 MPa 15  $\mu\text{m}$

2. Instrumentation

- one central thermocouple, sheathed, ungrounded junction
- four fast film thermocouples cemented on outer aluminum surface

3. Heat transfer

- Equilibration time after reactor pulse 10 s
- calculated heat losses after 10 s for 2000 J energy deposition

convection	none
radiation	.1%
conduction	.5%

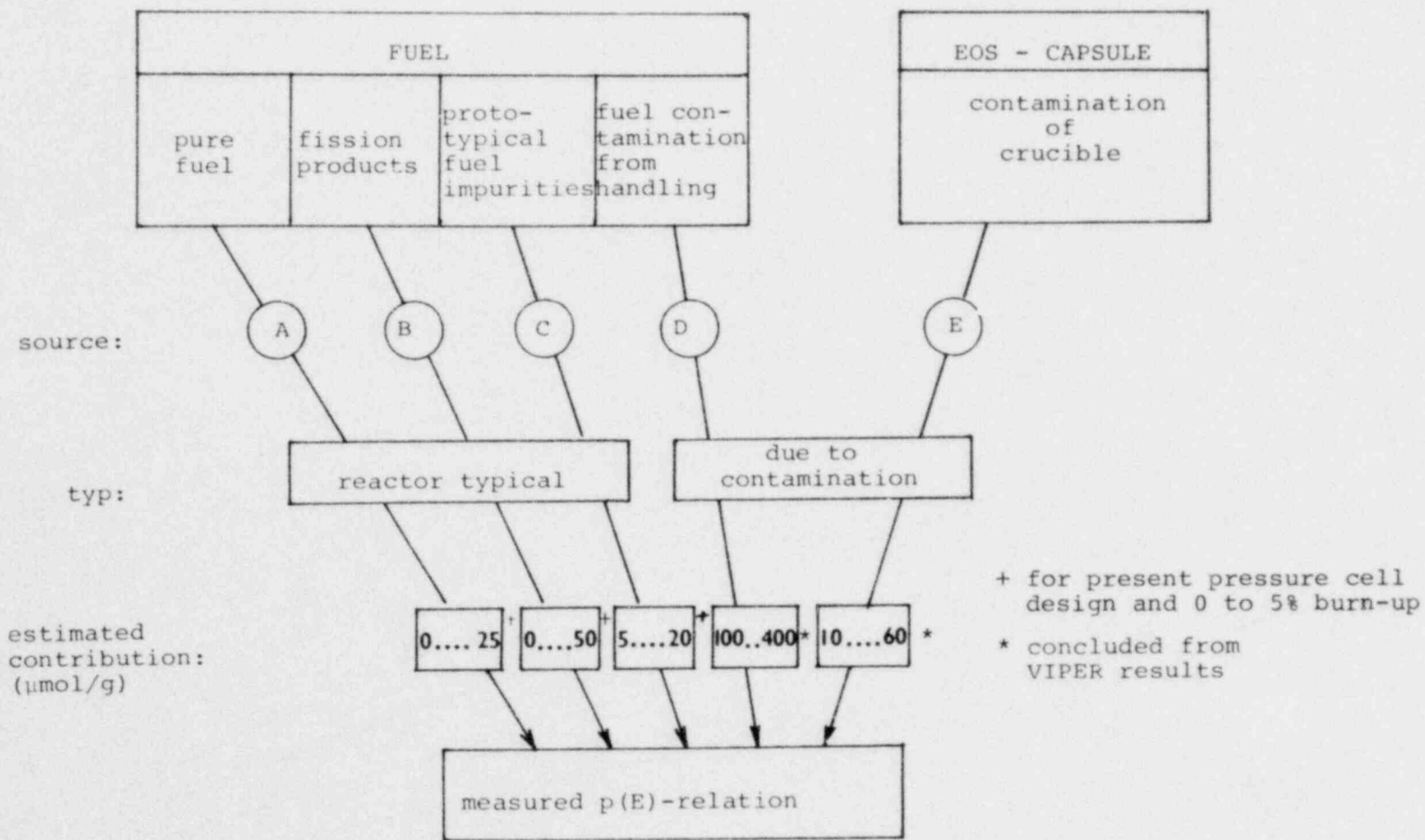
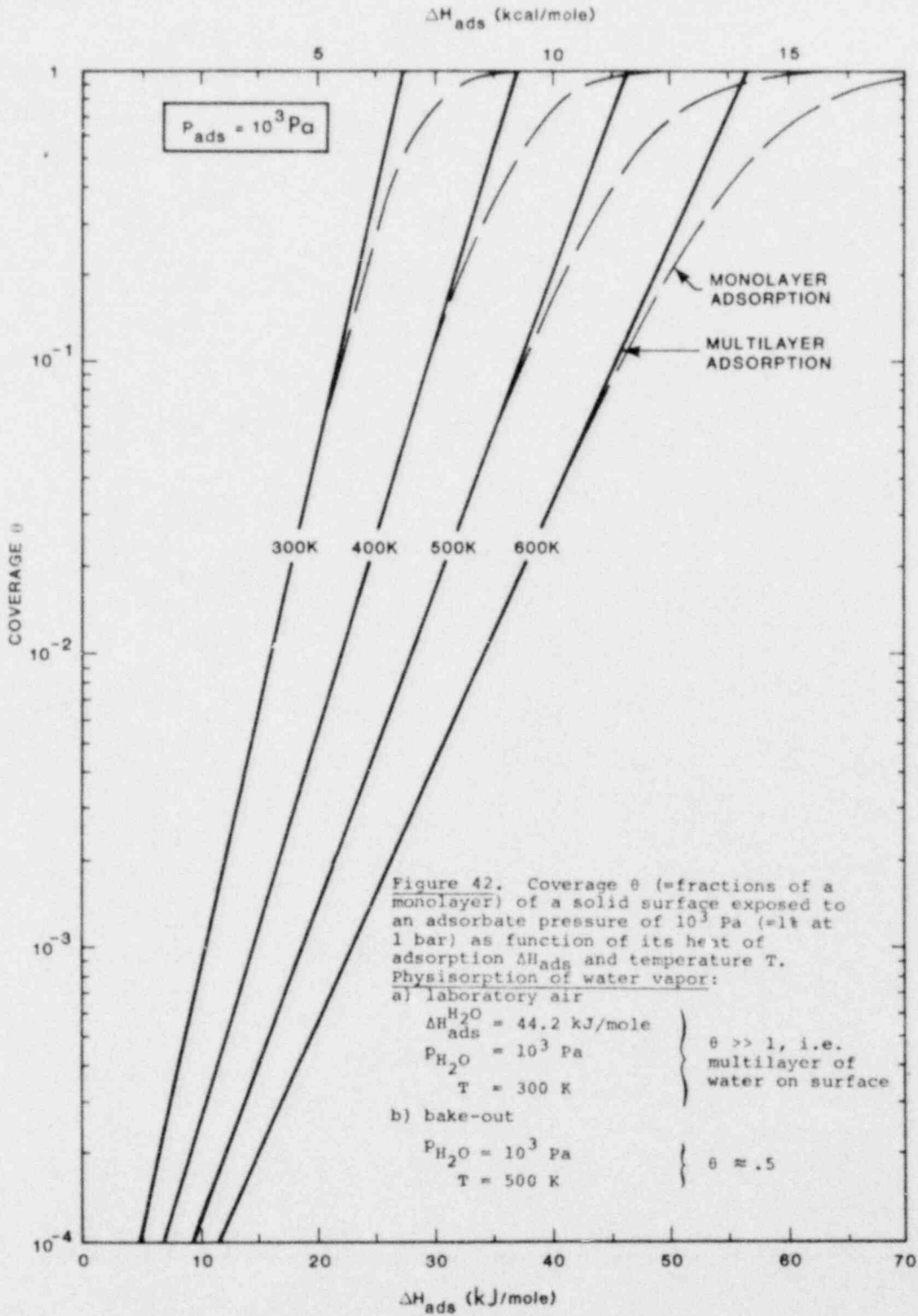


**Figure 41.** Pressure Sources Contributing to Measured p(E)-relation





Contamination Source and Expected Contaminants	Primary Cleaning	Secondary Cleaning (combined with storage)	Final Cleaning
<p>1. Contact contamination:  gross hydrocarbons    A  inorganic salts        B  particulates            C</p>	<p>Mechanical cleaning in water-ethanol, affected: B,C</p> <p>Ultrasonic cleaning in trichlorethylene, affected: A,F</p>	<p>UV-ozone cleaning supported by active adsorbents for water and hydrocarbons</p> <p>affected contaminants: E,F</p>	<p>heating in UHV-system to 500 K</p> <p>affected contaminants: E,F</p>
<p>2. Airborne contamination:  particulates            D  water                    E  film hydrocarbons      F</p>	<p>Ultrasonic cleaning in water-ethanol, affected: B,C,D</p> <p>UV-ozone cleaning prior to outgassing affected: A,F</p>		
<p>3. Bulk gases            G</p>	<p>Outgassing in vacuum affected: G</p>		

Figure 43. Summary of Cleaning Steps for EOS Pressure Cell Components

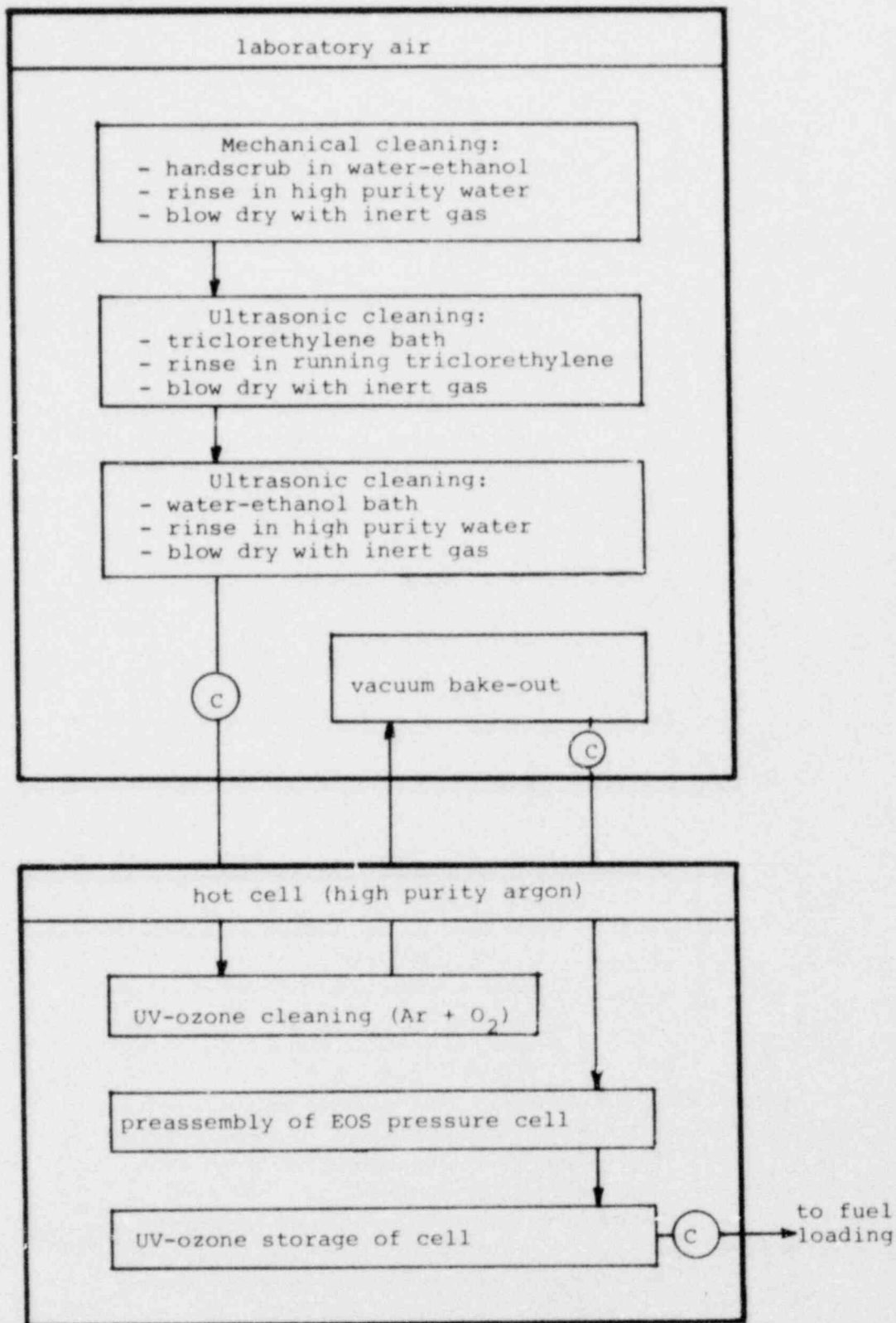


Figure 44. Flow of pressure cell components. © = most important points of contamination control.

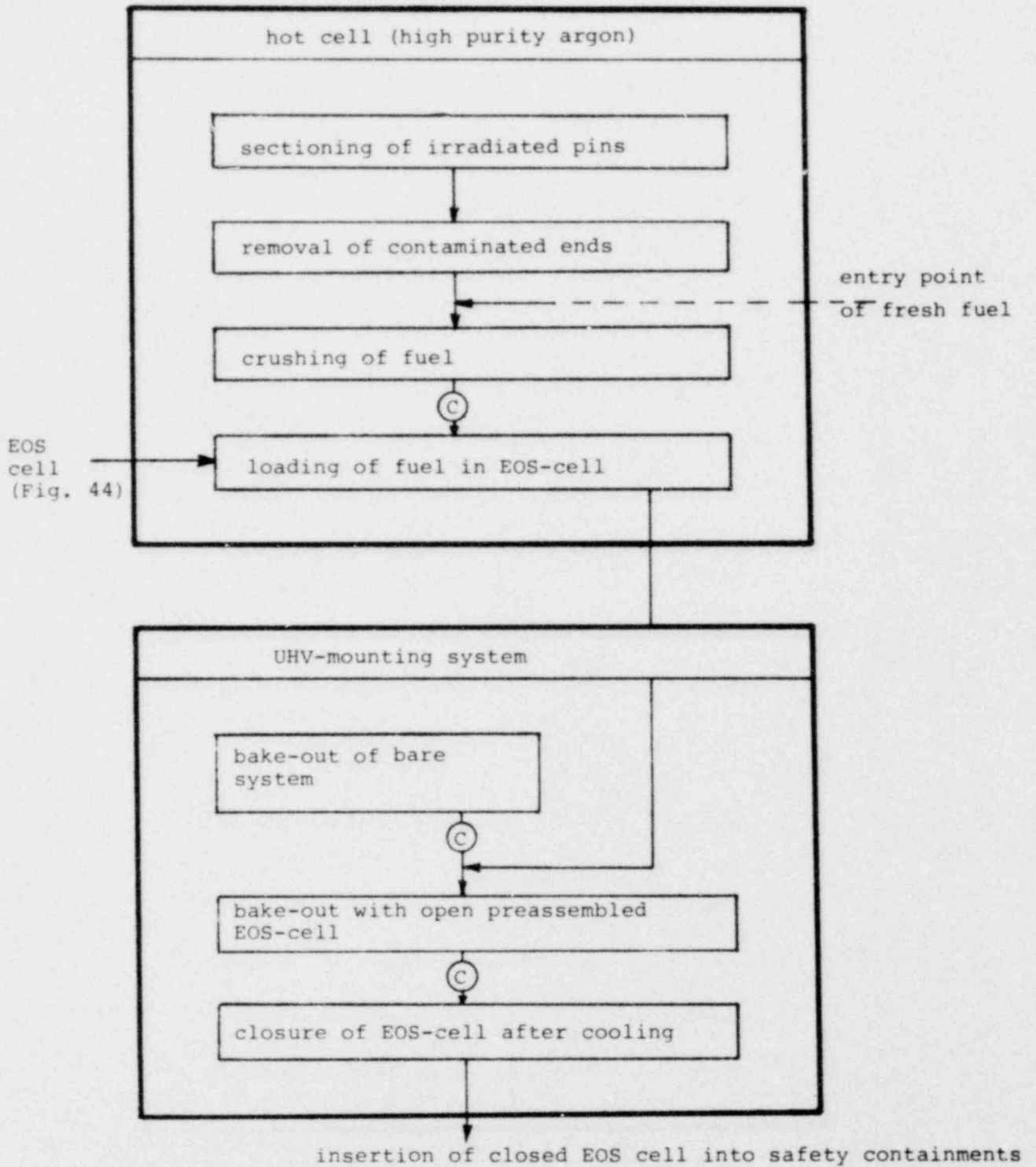


Figure 45. Flow of fuel and loaded EOS-cell. © = most important points of contamination control.

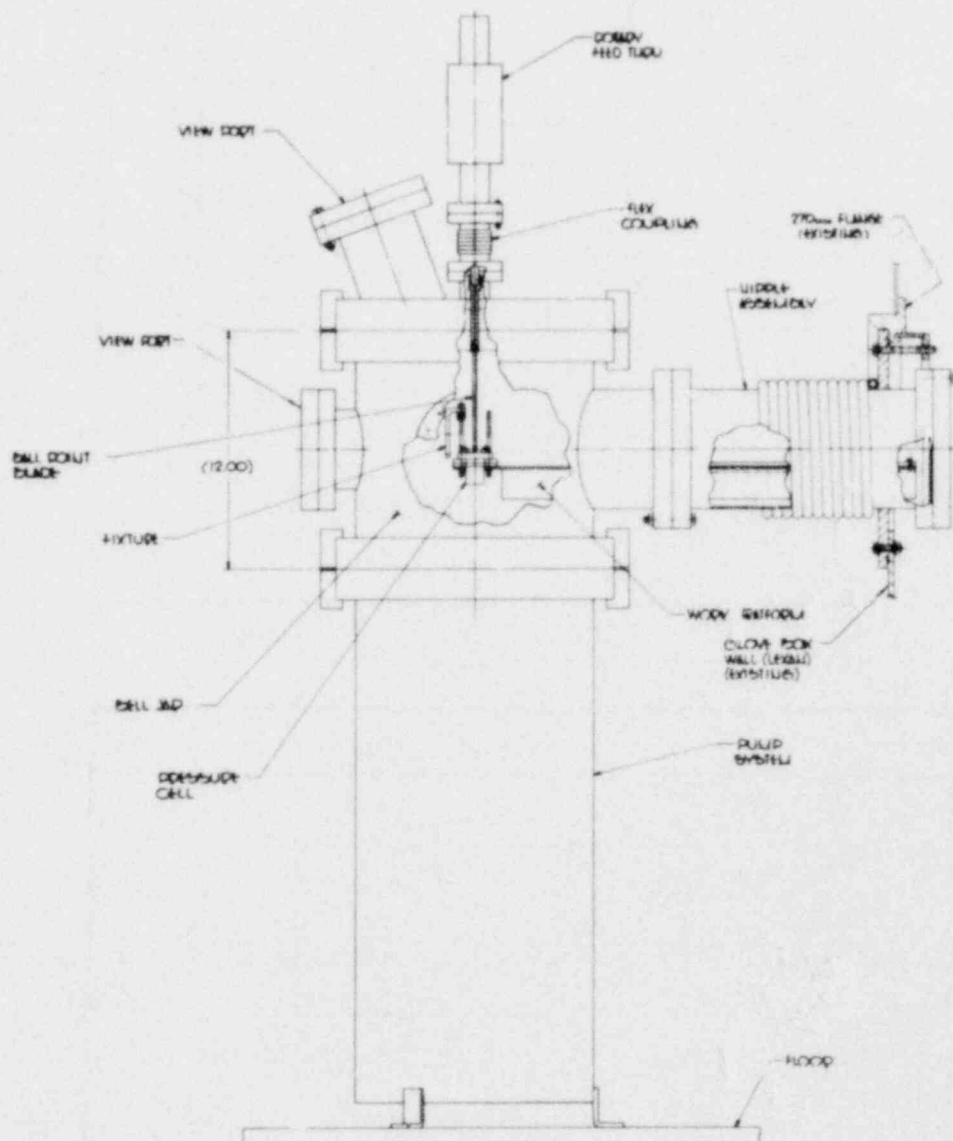
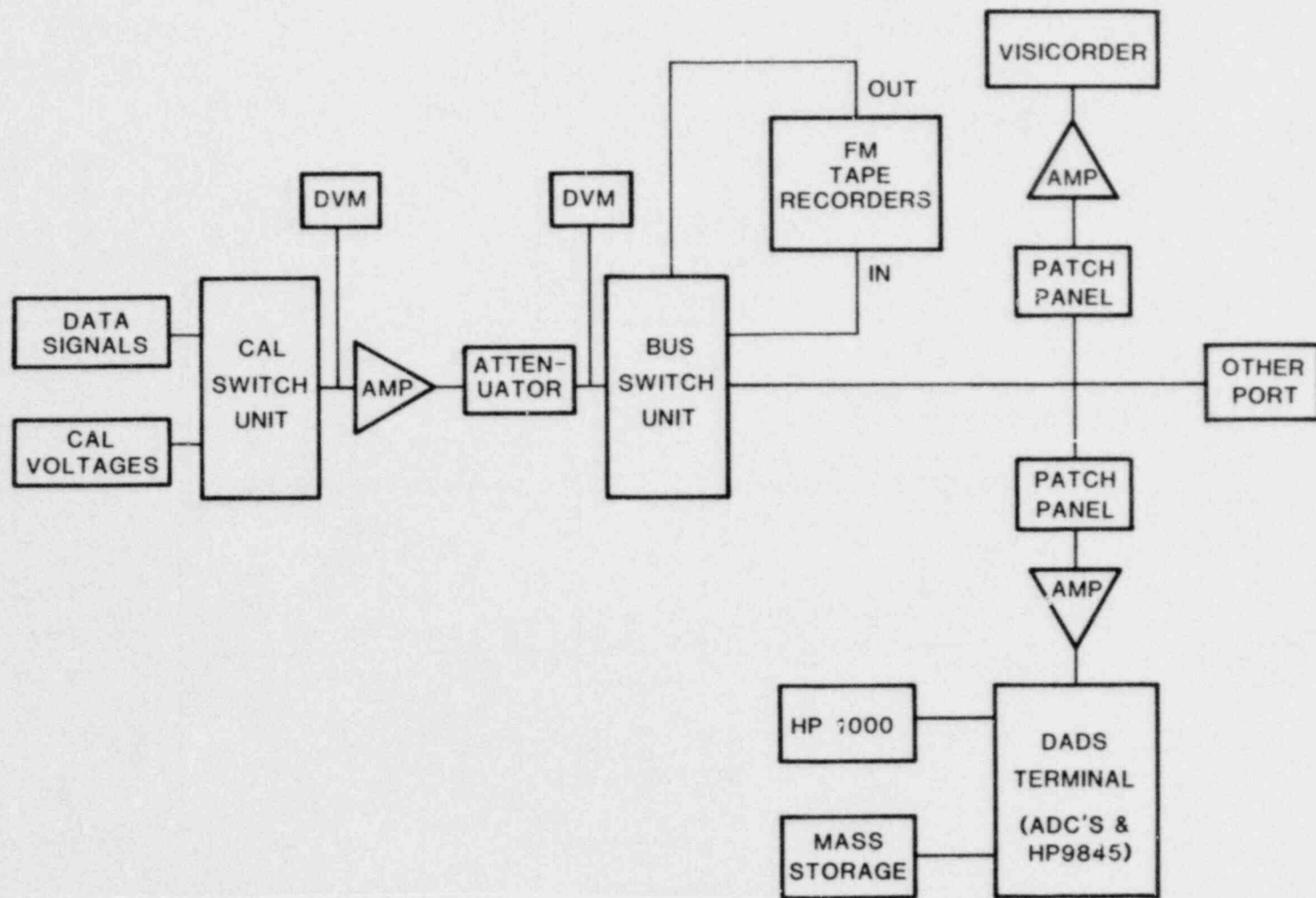


Figure 46. UHV-mounting system for bake-out, EOS cell closure and opening of pressure cell after the experiment for residual gas analysis.



-75-

FIGURE 47. BLOCK DIAGRAM OF DATA ACQUISITION SYSTEM.

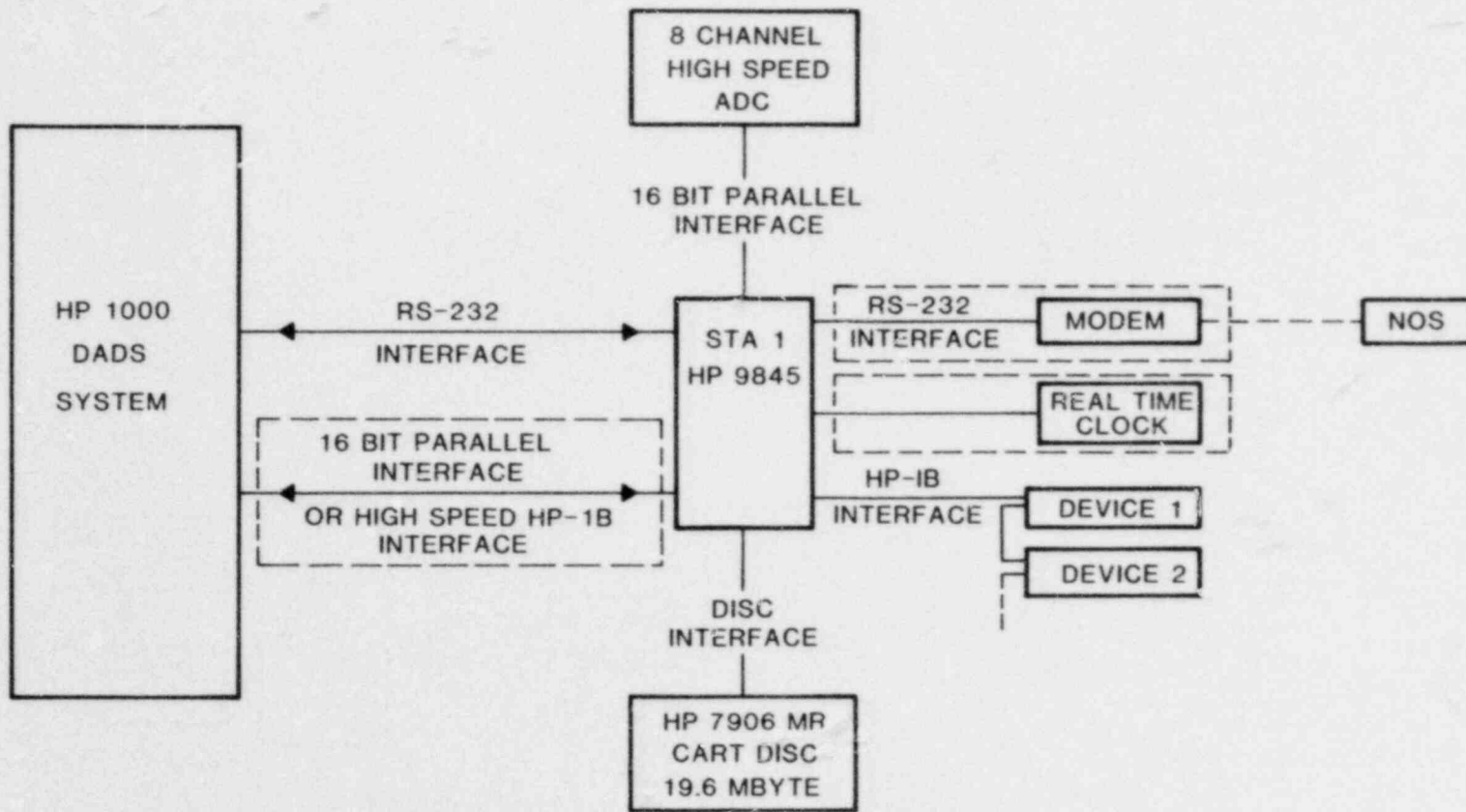


FIGURE 48. CONFIGURATION OF DADS STATION 1 (ACRR Low Bay) FOR CURRENT ACCIDENT ENERGETICS WORK (ITEMS IN DASHED BOXES DO NOT NOW EXIST).

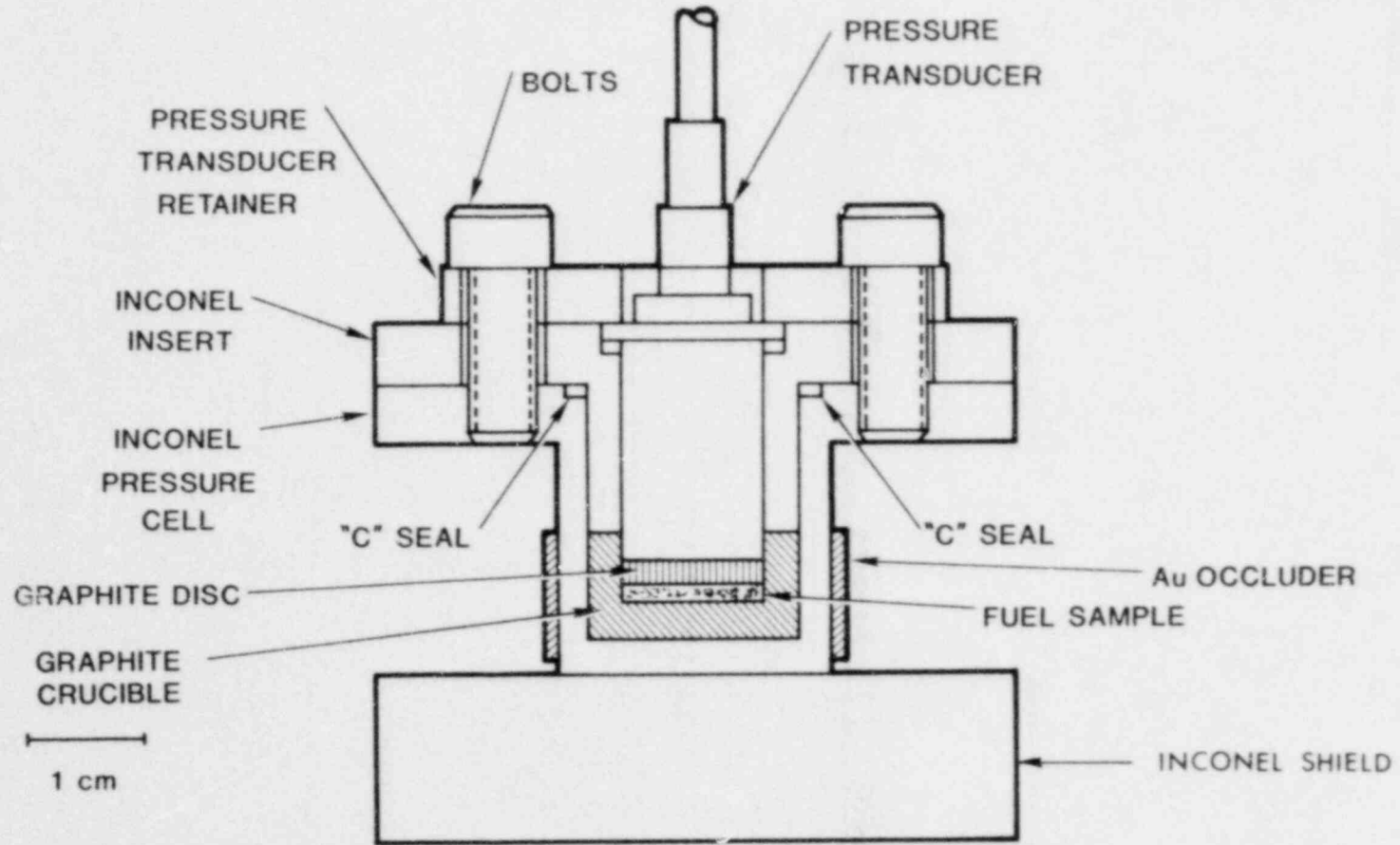


FIGURE 49. CROSS-SECTION OF EEOS PRESSURE CELL EQUIPPED WITH NEUTRON FILTERS.



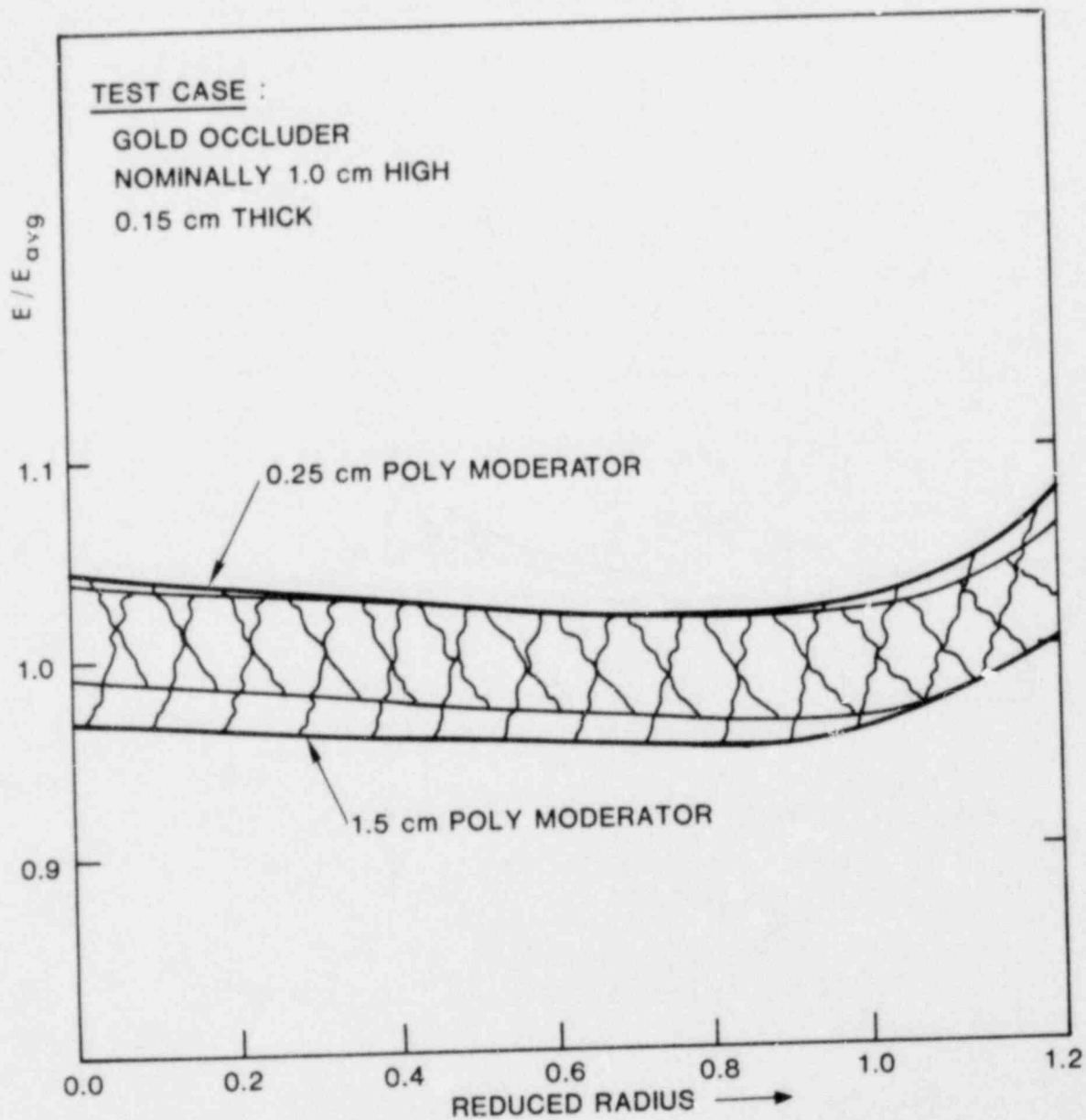


FIGURE 50. RELATIVE ENERGY DEPOSITION IN A FUEL POWDER DISK OF 50% THEORETICAL DENSITY. (UC, 1 G, 15% ENRICHED). CALCULATED PEAK-TO-AVERAGE RATIO IS 1.06 AND 1.07, RESPECTIVELY.

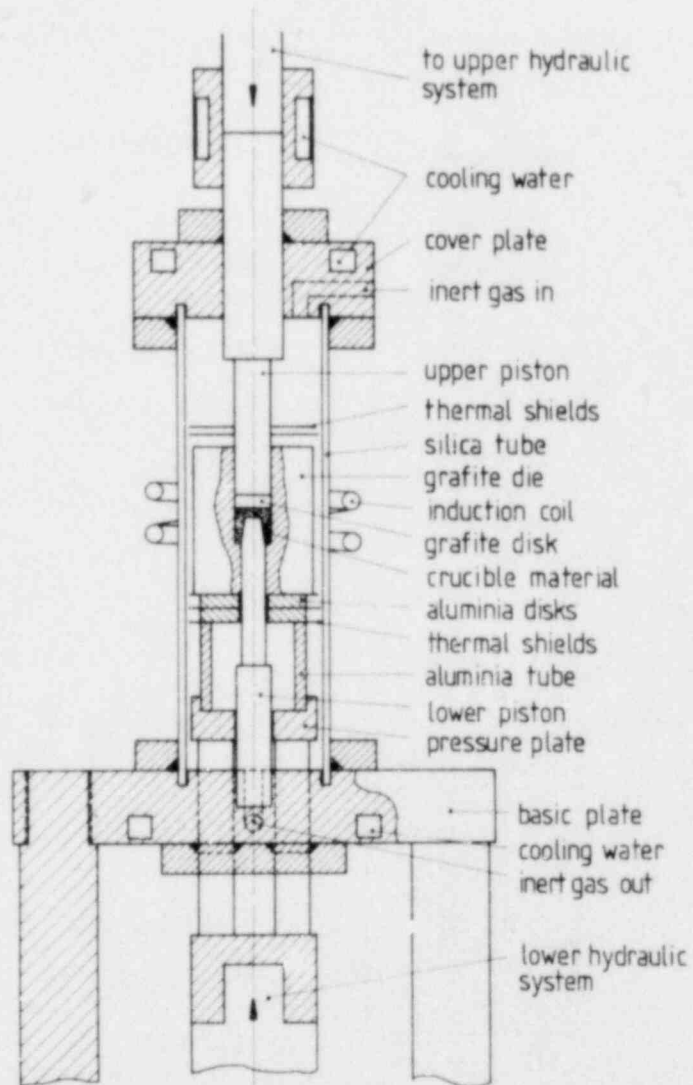
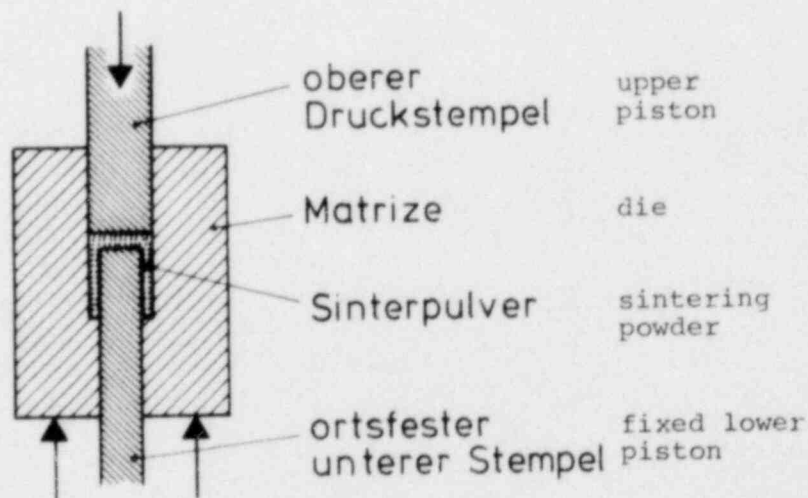
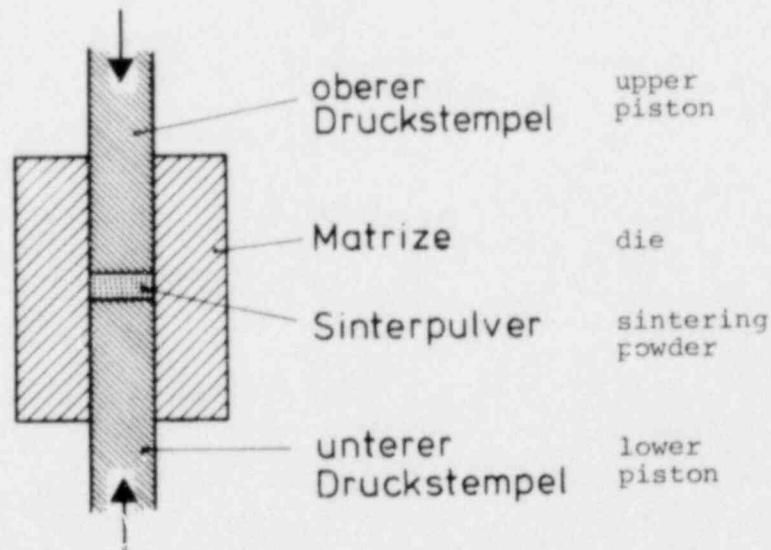


Figure 51. Elevation of Hot Pressing Apparatus



**Figure 52.** Fabrication principle for disks and crucibles. In the case of crucibles downward movements of the upper piston against the lower fixed piston compact the crucible bottom. Upward movements of the die compact the crucible walls.

pressures:	100 ... 150 MPa
temperatures:	about 2000 K
times:	about 5 min

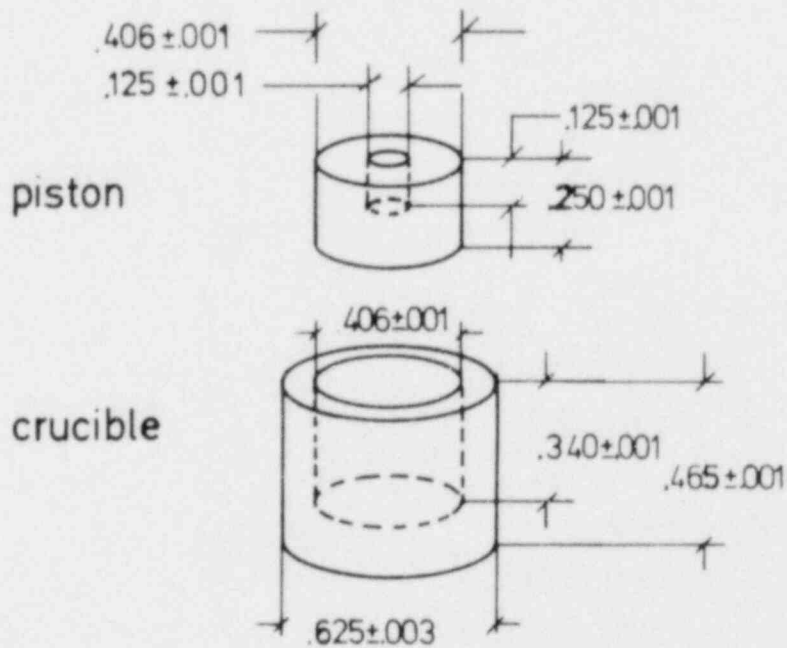


Figure 53. Dimensions of hot pressed  $\text{UO}_2$  crucible and  $\text{UO}_2$  piston in inch.

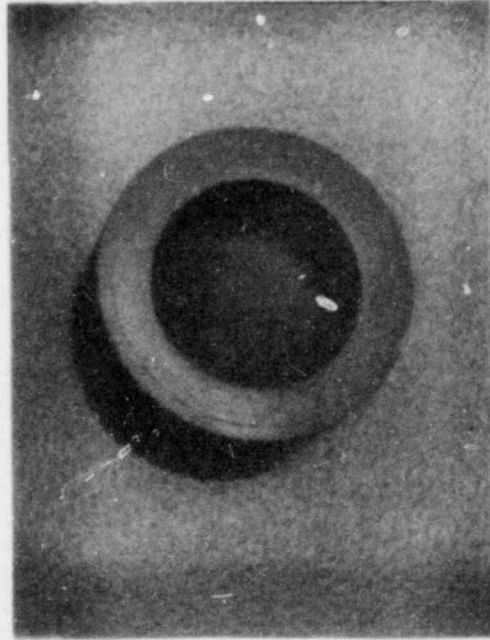


Figure 54. High density UO<sub>2</sub> crucible fabricated with the Hot Pressing Apparatus shown in Figure 51.

DISTRIBUTION:

U. S. Nuclear Regulatory Commission  
(380 copies for R7)  
Division of Document Control  
Distribution Services Branch  
7920 Norfolk Avenue  
Bethesda, MD 20014

U. S. Nuclear Regulatory Commission (4)  
Division of Reactor Safety Research  
Office of Nuclear Regulatory Research  
Washington, DC 20555  
Attn: C. N. Kelber, Assistant Director,  
Advanced Reactor Safety Research  
R. T. Curtis, Chief  
Analytical Advanced Reactor Safety Research, ARSR  
M. Silberberg, Chief  
Experimental Fast Reactor Safety  
R. W. Wright  
Experimental Fast Reactor Safety

U. S. Department of Energy  
Office of Nuclear Safety Coordination  
Washington, DC 20545  
Attn: R. W. Barber

U. S. Department of Energy  
Albuquerque Operations Office  
P. O. Box 5400  
Albuquerque, NM 87185  
Attn: J. R. Roeder, Director  
Operational Safety Division  
D. K. Nowlin, Director  
Special Programs Division  
For: C. B. Quinn  
D. Plymale

University of Michigan  
Nuclear Engineering Department  
Ann Arbor, MI 48104

Kernforschungszentrum Karlsruhe GMBH (25)  
Postfach 3640  
D75 Karlsruhe  
West Germany  
Attn: W. Marth, PSB  
G. Heusener, PSB (2)  
G. Kessler, INR  
M. Kuechle, INR  
K. Schretzmann, INR  
G. Schumacher, INR (5)  
M. Bober, INR

H. Werle, INR  
R. Froehlich, INR  
E. A. Fischer, INR  
H. Jacobs, INR  
G. Kleinheins, INR  
P. Schmuck, INR  
C. Essig, INR  
R. Dusing, INR  
D. Smidt, IRE  
P. Royl, IRE  
D. Struwe, IRE  
M. Cramer, IRE  
W. Zimmerer, IRE

Safety Studies Laboratory (2)  
Commissariat a L'Energie Atomique  
Centre d'Etudes Nucleaires de Cadarache  
B. P. 1  
13115 Saint Paul lez Durance  
France  
Attn: J. Wolff  
E. Bergeron

UKAEA (2)  
Safety and Reliability Directorate  
Wigshaw Lane  
Culcheth  
Warrington, WA3 4NE  
United Kingdom  
Attn: M. Hayns  
D. MacInnes

AERE Harwell (2)  
Oxfordshire, OX11 0RA  
United Kingdom  
Attn: R. G. Bellamy, Reactor Fuels Group  
J. R. Findlay, Applied Chem. Division

R. G. Tyror, Head  
Reactor Development Division  
UKAEA - Atomic Energy Establishment  
Winfrith, Dorchester  
Dorset  
England

M. H. McTaggart  
AWRE  
Aldermaston, Berkshire  
United Kingdom

Joint Research Centre (2)  
Ispra Establishment  
21020 Ispra (Varese)  
Italy  
Attn: R. Klersy  
H. Holtbecker

Power Reactor & Nuclear Fuel (3)  
Development Corporation (PNC)  
Fast Breeder Reactor Development Project (FBR)  
9-13, 1-Chome, Akasaka  
Minato-Ku, Tokyo  
Japan  
Attn: Dr. Mochizuki  
Dr. Watanabe (2)

1100 C. D. Broyles  
Attn: J. D. Kennedy, 1110  
T. L. Pace, 1120  
G. L. Ogle, 1125

1537 N. R. Keltner  
1537 R. U. Acton  
1537 T. Y. Chu  
1550 F. W. Neilson  
Attn: O. J. Burchett, 1552  
J. H. Gieske, 1552

2150 C. B. McCampbell  
3434 B. N. Yates  
4000 A. Narath  
4231 J. H. Penken  
4400 A. W. Snyder  
4410 D. J. McCloskey  
4420 J. V. Walker (5)  
4421 R. L. Coats  
4421 J. E. Gronager  
4421 G. W. Mitchell  
4421 J. B. Rivard  
4422 D. A. Powers  
4422 J. E. Smaardyk  
4422 D. W. Varela  
4423 P. S. Pickard  
4423 A. C. Marshall  
4423 D. A. McArthur  
4423 K. O. Reil (5)  
4424 M. J. Clauser  
4424 J. T. Hitchcock  
4424 P. J. McDaniel  
4424 M. E. Senglaub  
4425 W. J. Camp  
4425 W. M. Breitung (5)  
4425 F. Briscoe  
4425 R. J. Lipinski



4425 P. Mast  
4425 K. K. Murata (5)  
4425 M. L. Schwarz  
4425 A. Suo-Anttila  
4425 M. F. Young  
4426 G. L. Cano  
4426 J. G. Kelly  
4426 H. L. Scott  
4426 K. T. Stalker  
4426 W. H. Sullivan  
4426 S. A. Wright  
4450 J. A. Reuscher  
4451 T. R. Schmidt  
4452 M. Aker  
4723 D. O. Lee  
5500 O. E. Jones  
5530 W. Herrmann  
5534 D. A. Benson  
5800 R. S. Claassen  
5820 R. E. Whan  
5822 K. H. Eckelmeyer  
5830 M. J. Davis  
5835 C. H. Karnes  
5846 R. A. Sallach  
5846 E. K. Beauchamp  
8266 E. A. Aas  
3141 T. L. Werner (5)  
3151 W. L. Garner (3)  
For: DOE/TIC (Unlimited Release)  
3154-3 R. P. Campbell (25)  
For: NRC Distribution to NTIS